Influence of Pyridine on the Unique Multi-Electron Redox Cycle of Nickel Diethyldithiocarbamate

by

Chase Sanders Richburg

A thesis submitted to the Graduate Faculty of
Auburn University
In partial fulfillment of the
requirements for the Degree of
Master of Science

Auburn, AL
August 3, 2019

Keywords: electrochemistry, nickel, diethylthiocarbamate, cyclic voltammetry, pyridine, electron transfer

Approved by

Byron H. Farnum, Chair, Assistant Professor of Chemistry and Biochemistry
David Stanbury, Professor of Chemistry and Biochemistry
Evert Duin, Professor of Chemistry and Biochemistry

Abstract

Nickel is an intriguing metal for use in multi-electron renewable energy storage due to its high earth-abundance and cost-effective nature. Understanding the redox chemistry of this metal could lead to better redox storage molecules for harvested renewable energy. Unlike traditional one-electron redox couples of first row transition metals, nickel dithiocarbamates exhibit a unique multi-electron redox cycle that could increase energy storage capabilities and power performance of redox flow batteries used for renewable energy storage. Herein, we report mechanistic insight to the nickel diethyldithiocarbamate ($Ni^{II}(dtc)_2$) redox cycle and characterization of high valent Ni^{III} and Ni^{IV} oxidation states of these complexes by in-depth chemical and electrochemical analyses. These results provide a greater understanding of what enables the unique $Ni^{II}(dtc)_2$ redox cycle and the conditions that drive these complexes to undergo one-electron or two-electron transfer reactions. Much of this information is gleaned from the inclusion of an ancillary ligand, pyridine, into the electrochemical cycle and understanding how pyridine enables stabilization of an interesting Ni^{III} intermediate. This greater understanding of Ni^{III} and Ni^{IV} chemistry is fundamental in nature and demonstrates the need for further exploration and application of dithiocarbamates in the field of renewable energy storage.

Acknowledgments

A couple years ago was the first time I heard the African proverb, “If you want to go fast, go alone. If you want to go far, go together.” By God’s grace and to the credit of the wonderful people around me, I say, with humility, that I have a foundation that will take me far in this life. I am deeply grateful for each person who has invested in me during the twenty-three years of my life, and though I cannot mention all of the teachers, professors, family, and friends who have influenced me for the better, this is my best attempt to show some of you a fraction of the honor you deserve. Together, you have made me who and where I am today.

Mom and Dad, I could not be prouder to call you my parents. You have loved me unconditionally and I strive to be like both of you in many ways. Dad, you have taught me to pursue excellence in all things for as long as I can remember, and you have instilled in me a love for the outdoors that I will enjoy in many ways forever. Mom, you serve the people you know so well. I’ve said before that you would leave what you are doing to help anyone, anywhere, at any time, with anything, even when it is not convenient for you. I thank you for my “chemistry brain!”

Riley and Bryce, you are great brothers, and coming home to see you throughout my time in college has helped me rest and recharge in a big way. I am proud of the men you are becoming. Our brotherhood has grown into friendship too; for this, I am thankful.

Nicole, my sweet bride and best friend, I think the world of you. Thank you for the support and encouragement you have provided to me during the last few years; I value your words more than any others. I am a better man because of you, and I pray God grants us many more years of

life together to learn, love, and grow alongside each other into the people he has intended for us to be. Life with you is fun!

Professor Farnum, when talking about you, some of your colleagues have said, “Some people were born to be an advisor.” I wholeheartedly agree. I have great respect for the way you have led our research group the past 2+ years and am excited to see the impactful research that will be accomplished in the coming decades under your direction. It has been cool being a part of your lab from its very formation and being mentored by you as an undergraduate in those early days. I would have never thought that my bike wreck in August of 2016 that connected us would have such a positive and profound impact! Blessings on you, Kathryn, and Olivia in the years to come.

Thank you, Dr. Evert Duin, for agreeing to be on my advisory committee, and for your time spent performing EPR experiments for this project. Dr. David Stanbury, thank you as well for being on my advisory committee, and for your insight into our stopped flow and NMR experiments. Dr. John Gordon and Dr. Soumen Saha, thank you for the time and energy spent collecting single crystal data.

To my research group: I cannot imagine having enjoyed my time in graduate school as much as I have if it were not for each of you. You are a diverse and gifted bunch! Alex, your intelligence and service to others will make you a great teacher and mentor one day. Motiur, Soumen, and Russel, thank you for sharing your culture and your lives with me; it has been an honor getting to know you “Deshi boys.” Amanda, Andricus, Noah, Javier, and Alex, we have shared many laughs and I am eager to see what each of you accomplish in the coming years. It’s been an honor being a “nickelboy.” To the community of my other friends in Auburn, thank you

for how you have loved and supported Nicole and me in life's best and worst. This life was not meant to be lived alone! Auburn is truly a special place because of you.

Finally, to the one, true God who makes life worth living, thank you. I had nothing to offer you when you captured my heart nearly ten years ago, yet you redeemed me, changed me, invited me into your grand story, and gave me a purpose. My heart has been freed, and there is nothing better than living life in your design! I am "fully convinced that you are able to do what you have promised!" *Maranatha,* come Lord Jesus!

Table of Contents

List of Tables

List of Figures and Schemes

List of Abbreviations

BPI	Bipyridylimino Isoindoline
C	Chemical-reaction step
CE	Chemical-reaction step followed by Electron-transfer step
CV	Cyclic Voltammogram/Voltammetry
DISP	Disproportionation
Dtc	Dithiocarbamate
E	Electron-transfer step
EC	Electron-transfer step followed by Chemical-reaction step
ECE	Electron-transfer step, Chemical-reaction step, Electron-transfer step
EE	Electron-transfer step followed by another Electron-transfer step
EPR	Electron Paramagnetic Resonance
GC	Glassy Carbon
HPLC	High Performance Liquid Chromatography
HSAB	Hard Soft Acid Base
IUPAC	International Union of Pure and Applied Chemistry
LCET	Ligand Coupled Electron Transfer
LiTFSI	Lithium bis(trifluoromethanesulfonyl)imide
MCC	Metal Coordination Complex
MeCN	Acetonitrile

PCET	Proton Coupled Electron Transfer
Py	Pyridine
NMR	Nuclear Magnetic Resonance
RFB	Redox Flow Battery
RDE	Ring Disk Electrode
RRDE	Rotating Ring Disk Electrode
RSD	Radical Substrate Dimerization
$TBAPF_6$	Tetrabutylammonium hexafluorophosphate
TMS	Tetramethylsilane
UV	Ultra Violet

Chapter 1: Introduction

Challenges in Energy Storage

The need for energy storage is greater than ever. The sheer amount of renewable energy available just in the United States in forms such as solar or wind power is staggering, as seen in **Figures 1.1** and **1.2**.[1,2] These figures demonstrate that the availability of solar energy is highest in the southwest portion of the country and wind speeds are fastest along the northeast coast, west coast, and central plains. Solar cell technologies used to harvest this energy such as multi-junction and perovskite cells have been consistently developing.[3] Despite the amount of available renewable energy on any given day, renewable sources such as solar and wind energy are intermittent, variable, and diffuse. This intermittency is shown in **Figure 1.3**, which illustrates the fluctuations in available solar energy in Alabama on July 2-3, 2006.[4] Thus, energy storage is a vital part of successful renewable energy implementation.

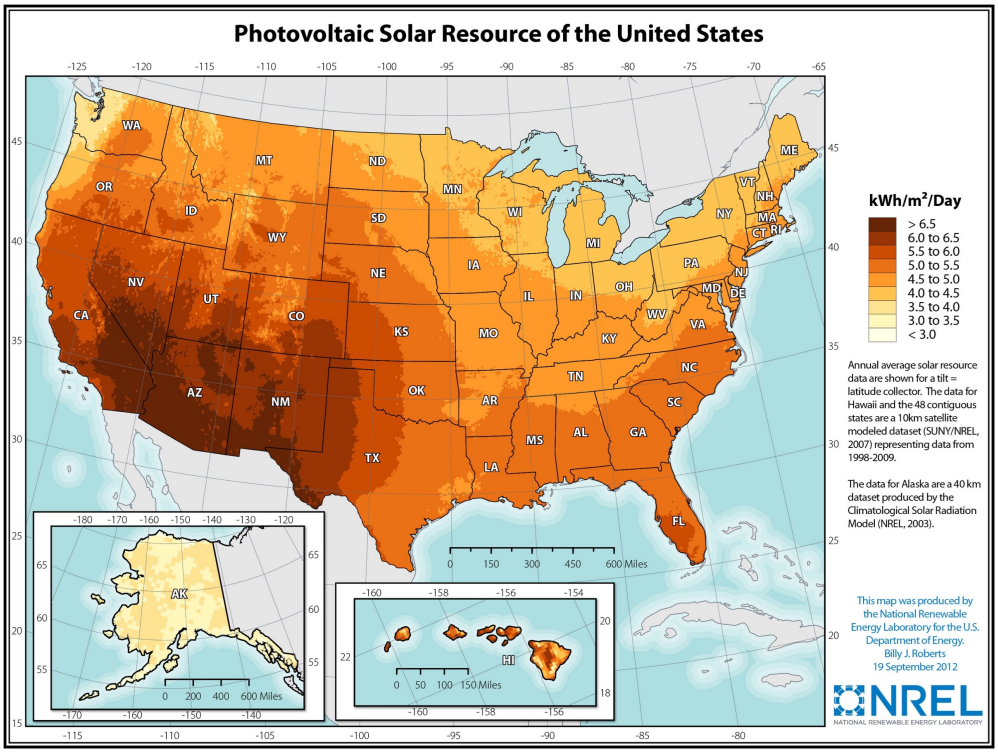

Figure 1.1. Photovoltaic solar resource of the United States[1]

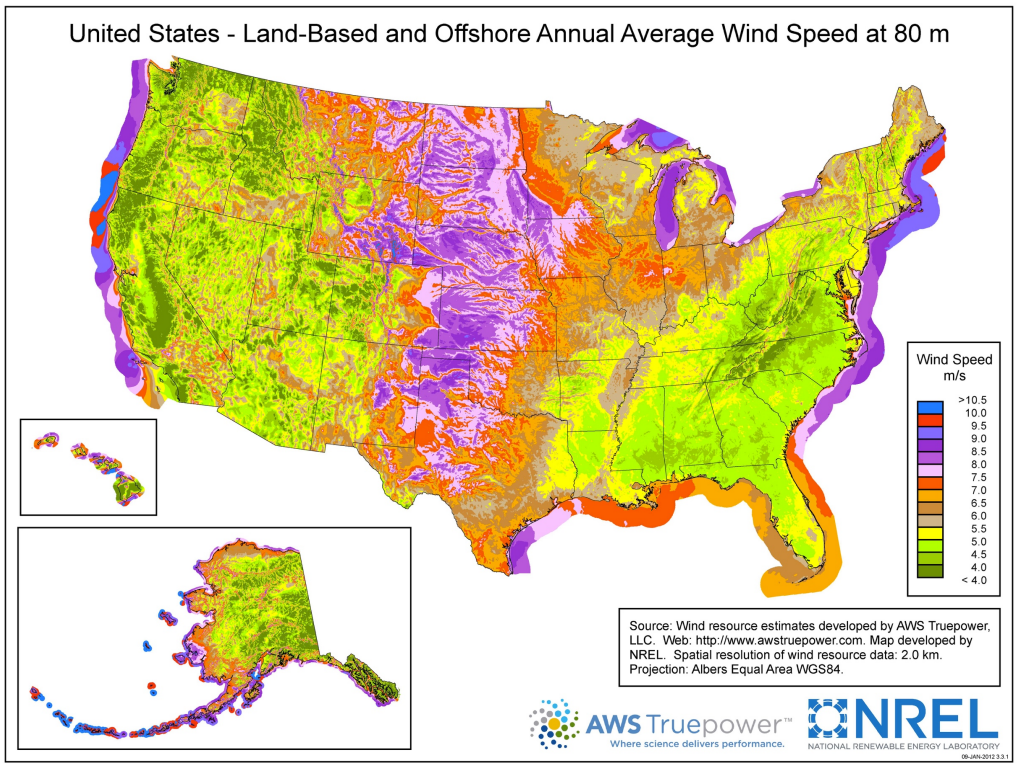

Figure 1.2. Land-based and offshore annual average wind speed at 80 m in U.S.[2]

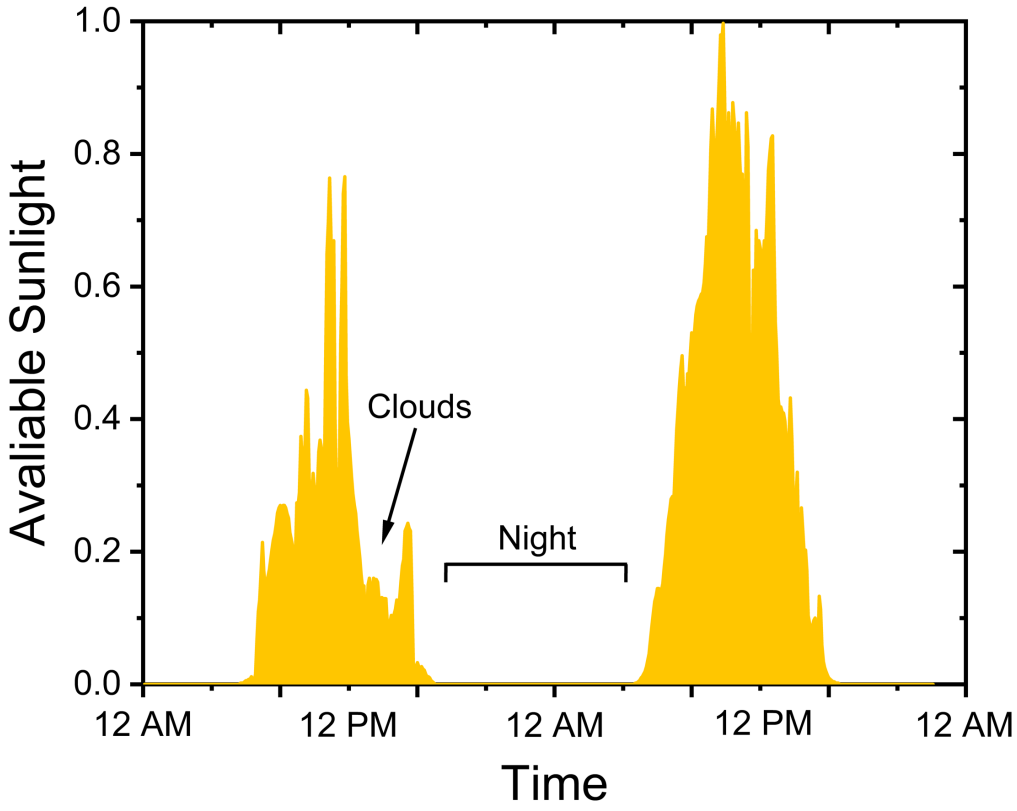

Figure 1.3. Normalized fluctuations in available solar energy for Alabama on July 2-3, 2006[4]

Progress in Energy Storage

The development of Redox Flow Batteries (RFBs) has been one of the primary responses to the need to store harvested renewable energy. In an RFB, the catholyte and anolyte are two electrolytes that contain redox active molecules. The catholyte contains molecules which are oxidized to store energy and reduced to release energy, whereas the anolyte contains molecules which are reduced to store energy and oxidized to release energy. Thus, these electrolytes are defined with respect to battery discharge.

The architecture and flow of redox-active molecules in an RFB can be seen in **Figure 1.4.** The catholyte and anolyte are stored in two distinct cells, the negative and positive cells, respectfully, and pumped from these storage tanks to what is labeled as the "regenerative fuel cell" upon demand. These storage tanks can be as small or large as desired, thus making scalability a major advantage of the RFB. Cells in RFBs can typically be classified as symmetric or asymmetric, where symmetric cells contain the oxidized and reduced forms of the same molecule in separate tanks, whereas asymmetric cells contain different molecules altogether in the positive and negative cells. Molecules used in symmetric RFBs must have at least two redox couples for a reaction to occur; a significant difference in potential between the oxidized and reduced forms of the molecule is best. An ion-selective membrane divides the fuel cell and prevents the two electrolytes from mixing and self-discharging. Controlled discharge of an RFB occurs when electrons flow from the anolyte, into the anode, across the load (where energy is extracted), and into the cathode, where the catholyte is then reduced. The difference in redox potentials between the catholyte and anolyte drives the movement of electrons and is defined as V_{cell}, where $V_{cell} = E_c - E_a$. When the redox reaction has run to completion, the battery may be recharged by reducing the anolyte and oxidizing the catholyte with energy input from a solar or wind resource.

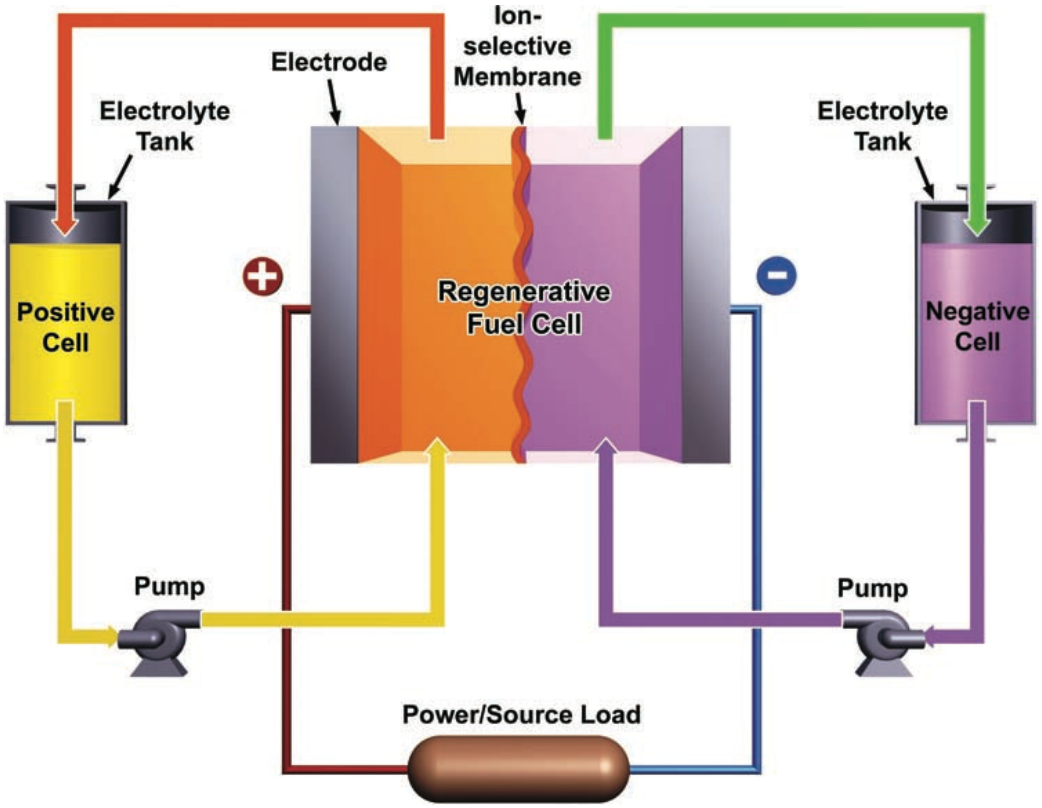

Figure 1.4. Illustration of a redox flow battery and its components. Reprinted from Graff *et al.*[5]

RFBs work similarly to rechargeable batteries and have the potential to be applied toward grid-scale energy storage. The energy density ($\hat{E}$) of an RFB is determined by **Equation 1**, where n is the number of electrons transferred, V_{cell} is the difference in redox potentials of catholyte and anolyte molecules, C_{active} is the average concentration of the two redox active species, and F is Faraday's constant:

$$\hat{E} = nV_{cell}C_{active}F \qquad (1)$$

Thus, the energy density can be increased by manipulating any one of the above variables. In an effort to increase V_{cell}, many scientists have begun developing RFBs for use in non-aqueous systems such as acetonitrile that are not limited by the small voltage window of water (1.23 V), yet one challenge that remains is developing molecules that can compete with the high solubilities

of some vanadium salts (~2 M) used in aqueous redox flow batteries.[5–7] Sanford *et al.* have taken a multistep approach to increase both V_{cell}, C_{active}, and n by designing a non-aqueous RFB containing fairly soluble metal coordination complexes (MCCs) with redox-active ligands capable of being oxidized and reduced over a voltage window of >1.23 V.[8,9] The most promising candidates in these studies were shown to be tris-bipyridine chromium complexes with ester substituents. These complexes have solubilities as high as 0.71 M in acetonitrile (MeCN) with six reversible redox couples over a ~2 V range. Therefore, these molecules could be used in a symmetrical RFB with an n = 2 or 3. However, these MCCs have a substantial capacity fade over the course of even 10 charge-discharge cycles in an electrochemical cell.

Sanford *et al.* then designed tridentate bipyridylimino isoindoline (BPI) ligands that also have multiple redox couples yet can undergo many charge-discharge cycles when complexed to certain metal centers.[10] In particular, the best candidates for use as an anolyte in an RFB in this study were found to be a nickel complex that had less than 5% capacity loss over 200 cycles, and another similar nickel complex that exhibits an impressive combination of a solubility greater than 0.7 M, multiple one-electron ($1e^-$) transfers at low redox potentials, and a high stability in the doubly reduced form for days at a time. Thus, nickel complexes containing redox-active ligands have been shown to be great candidates for use as anolytes in which ligand-based reduction is responsible for energy storage. Despite how effective nickel based MCCs can be as redox active species in RFBs, there is not a single example in the literature of a nickel MCC being used as a catholyte. Such a molecule would require redox events at the metal center to be active toward energy storage.

Two-Electron Chemistry

Molecules having two, sequential 1 e^- redox events certainly can be advantageous for use in RFBs compared to molecules with one redox event. Indeed, the MCC molecules described above adhere to this strategy. However, peak power output can be increased by as much as 30% when the redox event is a two-electron ($2e^-$) transfer at a single potential. This can be seen in **Figure 1.5**, which shows sample iV curves for two systems: a molecule that has one, $2e^-$ redox couple (red) and a molecule that has two, $1e^-$ couples (blue). Note that the average reduction potential of the $1e^-$ couples was equal to the single $2e^-$ couple.

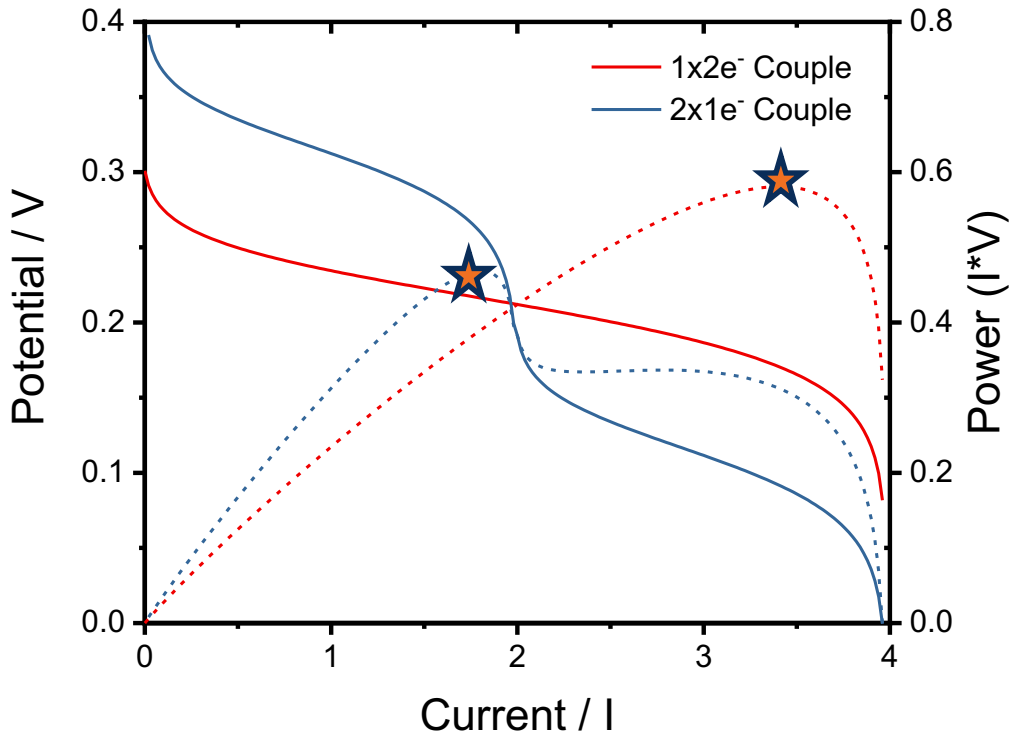

Figure 1.5. Battery voltage (solid) and electrical power (dashed) plotted as a function of charge/discharge current for two redox systems: a single $2e^-$ couple (red) vs two $1e^-$ couples (blue)

Thus, a greater knowledge of what enables $2e^-$ transfer chemistry would benefit the field of RFBs. There are few, true examples of metal-based $2e^-$ transfer chemistry in the literature. In order to see a reversible redox wave corresponding to a $2e^-$ couple, it first requires inversion of

reduction potentials. For example, oxidation of M^{II} to $M^{IV}L_2$ represented by E_3^o in **Figure 1.6** can be observed electrochemically when E_2^o becomes more negative than E_1^o, where L represents a ligand binding to the metal center. In this case, $M^{III}L$ is highly unstable, yet the oxidized M^{IV} state is able to be stabilized by the coordination of 2 L, generating potential inversion. This process, referred to as Ligand Coupled Electron Transfer (LCET), is complementary to that of Proton Coupled Electron Transfer (PCET), where electron reduction results in the formation of a chemical bond to H^+. Thus, coupling electron transfer with chemical bond formation enables control of reduction potentials and promotes $2e^-$ reactivity.

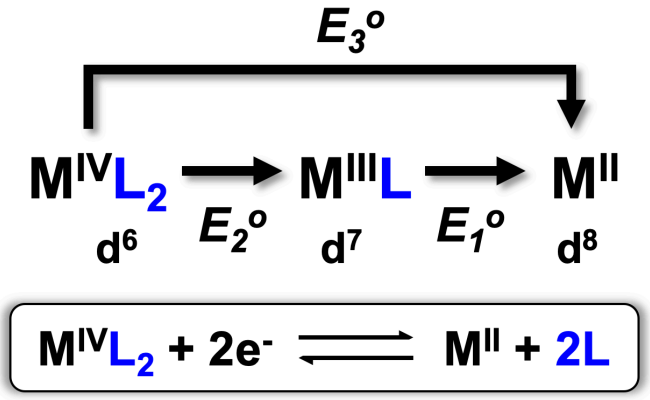

Figure 1.6. Latimer diagram for $2e^-$ transfer reaction at metal "M"

There are two main types of electron transfer: outer-sphere and inner-sphere electron transfer. Outer-sphere electron transfer refers to an electron transfer event that occurs between chemical species that remain unchanged throughout the course of the electron transfer event. Inner-sphere electron transfer refers to the participating redox sites in a molecule being joined by a chemical bridge (i.e. reductive elimination and oxidative addition). Inner-sphere $2e^-$ transfer at transition metals is well documented, as nearly any catalytic reaction that uses a metal center as a catalyst exhibits inner-sphere $1e^-$ or $2e^-$ transfer, but few true outer-sphere $2e^-$ transfer examples have been shown.

Connick *et al*. reported a platinum complex that undergoes an outer-sphere $2e^-$ transfer from Pt^{II} to Pt^{IV}.[11] This transformation happens through the unique ability of both terpyridyl and pip_2NCN^- (1,3-bis(piperidylmethyl)benzene) ligands to stabilize the Pt^{IV} center through lone electron pairs on the piperidyl nitrogens. Other noteworthy outer-sphere $2e^-$ transfer examples, yet with the first-row transition metal cobalt, have been shown by Saveant, Lever, and Waymouth. Saveant and Lever demonstrated that cobalt is capable of $2e^-$ transfer at the metal center when cyanide or hydroxide acts as a coordinating ligand.[12,13] Waymouth recently reported a cobalt phenylazopyridine complex that has a $Co^{III/I}$ wave at just -0.16 V. vs. $Fc^{+/0}$ in MeCN.[14] Thus, little is known about the conditions needed to drive outer-sphere $2e^-$ transfer in first-row transition metals.

One final example of $2e^-$ chemistry is the iodide/triiodide redox couple (I^-/I_3^-).[15] The balanced redox reactions for this redox couple can be seen in **Equations 2-3**.

$$I_3^- + 2\ e^- \rightleftharpoons 3\ I^- \qquad (2)$$

$$3\ I_2 + 2\ e^- \rightleftharpoons 2\ I_3^- \qquad (3)$$

Although iodide is not a transition metal, the same principles of LCET described above can be applied to this multi-electron redox system. Namely, oxidation of iodide is coupled to chemical bond formation and reduction of triiodide is coupled to chemical bond cleavage.[16–19] In a cyclic voltammetry (CV) experiment (the basic principles of which will be discussed later in this chapter), both the I^-/I_3^- and I_3^-/I_2 redox couples can be observed. Despite each of these waves being a $2e^-$ process, net, less than two electrons are transferred per iodide because multiple I^- are involved in the transfer of multiple electrons; one I^- is oxidized and other I^- bind to it. Nonetheless, the waves corresponding to these redox couples are $2e^-$ in nature and can be seen in **Figure 1.7.** The

I^-/I_3^- redox couple is currently used in RFBs as a catholyte,[20–23] yet there are currently no $2e^-$ metal-based RFBs.

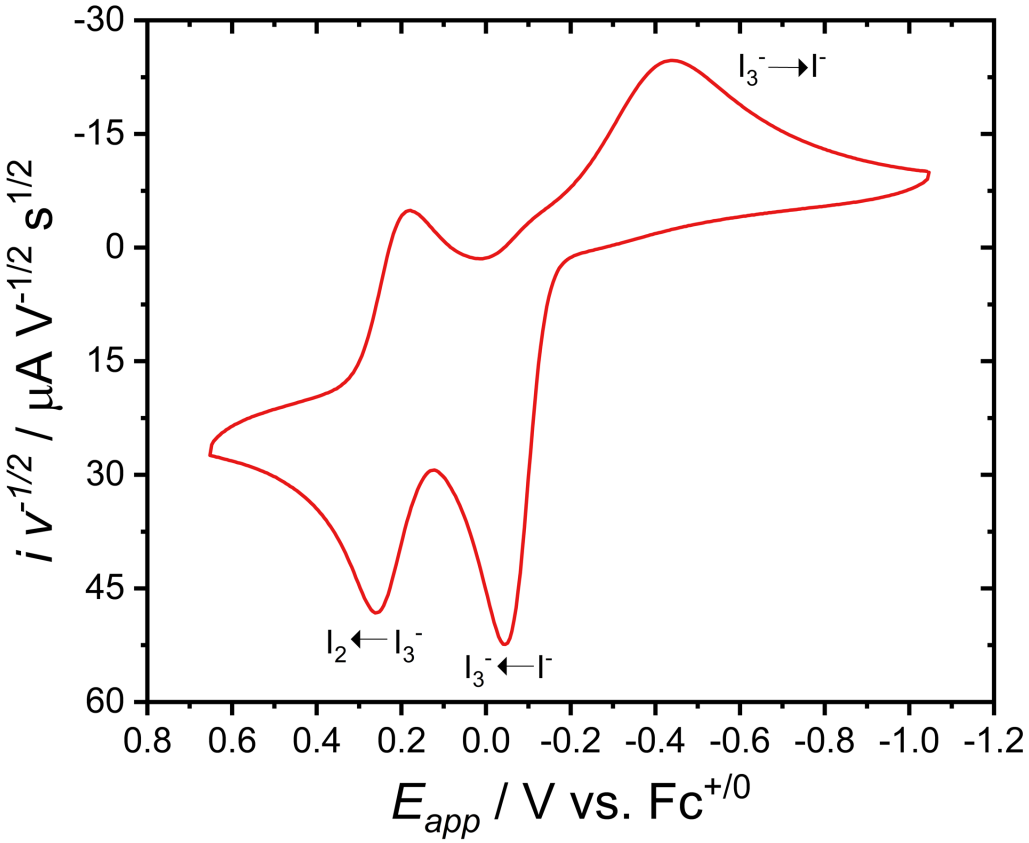

Figure 1.7. CV of 1 mM iodide in MeCN, 0.1 V/s, 0.1 M $TBAPF_6$ (tetrabutylammonium hexafluorophosphate), Pt working electrode

Nickel Dithiocarbamates

Nickel dithiocarbamates represent a unique class of MCCs. Hard Soft Acid Base (HSAB) theory predicts that relatively soft-intermediate Ni^{II} ion would pair well with the soft-intermediate dithiol group on the dithiocarbamate (dtc) ligand, and this is what is observed experimentally. The sulfur atoms on the dithio ligands are strong π-donors to the metal center and result in the molecule having a strong preference for a square planar environment. Axial coordination is resisted in the Ni^{II} state; however, these complexes undergo transformation to a tris-chelated Ni^{IV} state upon

electrochemical or chemical oxidation with Br_2 or acetylferrocenium ($AcFc^+$). Both Ni^{II} and Ni^{IV} oxidation states have been characterized by solution and solid state methods.[24,25] The only other examples of $Ni^{IV/II}$ electrochemistry seen in the literature are nickel oxime molecules in aqueous solution. Here, the Ni^{II} and Ni^{IV} states are both present in octahedral geometries, therefore, metal-ligand bond formation is not responsible for the observed $2e^-$ chemistry.[26] Instead, protonation of oxime ligands drives $2e^-$ chemistry at acidic pH conditions via PCET. Thus, the conversion between the square planar Ni^{II} dithiocarbamates and octahedral Ni^{IV} dithiocarbamates is unique and a large part of the driving force for $2e^-$ transfer in the dithiocarbamate redox system.

The stabilization of Ni^{IV} in the presence of sulfur containing ligands is notable given the propensity of sulfur to undergo radical oxidation. The ability of the 1,1-dithio functional group to support Ni^{III} and Ni^{IV} states stands in contrast to similar 1,2-dithio functional groups. Gray *et al.* have shown that molecules with 1,2-dithio functional groups instead have Ni^{II} metal centers, and rather, oxidized ligands by formation of a radical.[27] A comparison of the 1,1-dithio and 1,2-dithio functional groups can be seen in **Figure 1.8.**

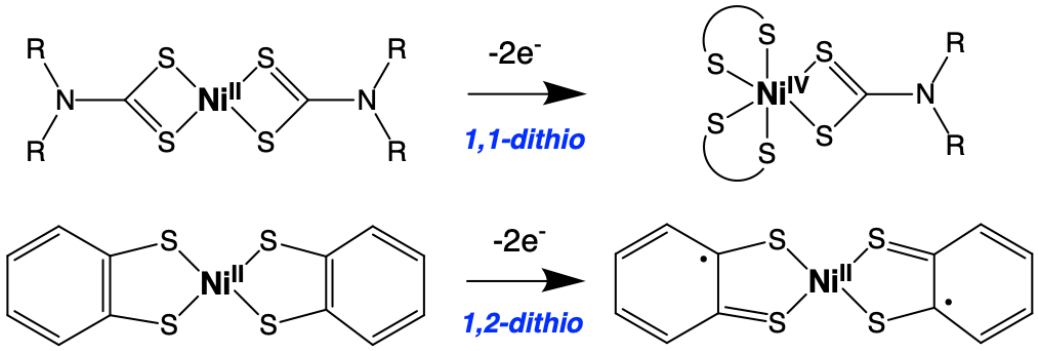

Figure 1.8. Comparison of the 1,1-dithio and 1,2-dithio functional groups upon oxidation

To date, there are few examples of stable, high valent nickel molecules, with one being a silyl complex[28] and many others being organometallic in nature.[29–38] Similar classes of ligands, such as the 1,2 dithio group, are not able to stabilize the Ni^{IV} state, but due to the resonance

capabilities of the 1,1 dithiocarbamate ligand, electron density can be shifted onto the sulfurs to stabilize the highly charged cation as shown in **Figure 1.9**. The increase in the resonance frequency of the C-N bond in $Ni^{II}(n\text{-}Bu_2dtc)_2$ upon oxidation to $[Ni^{IV}(n\text{-}Bu_2dtc)_3]^+$ from 1505 cm^{-1} to 1545 cm^{-1} indicates the stronger double bond character and greater electron density on the sulfur end of the molecule.[39] The general structure of nickel dithiocarbamates, as well as an illustration of the resonance capability of the 1,1-dithio ligands can be seen in **Figure 1.9**.

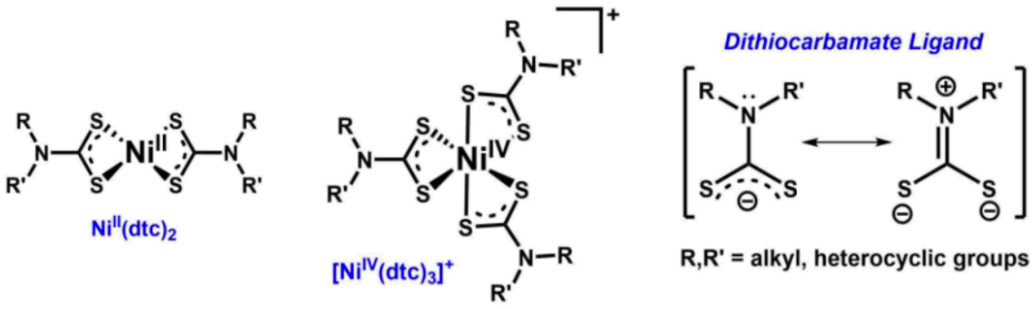

Figure 1.9. Bis and tris nickel dithiocarbamates and resonance of the 1,1-dithio ligand

Another fascinating characteristic of nickel dithiocarbamates is the reproducible, $2e^-$ redox cycle. The first electrochemical studies on $Ni^{II}(dtc)_2$ were performed by Hendrickson and Lachenal in 1975,[40,41] and the data supported the chemical oxidation studies performed several years earlier by Brinkoff and Fackler.[24,25,39] This reproducible redox cycle includes both EC and ECE mechanisms, where E represents an electron transfer step and C represents a chemical reaction step. In a CV, the bis-chelated nickel complex, $Ni^{II}(dtc)_2$, undergoes an ECE reaction and is oxidized by $2e^-$ *irreversibly* to the tris-chelated complex, $[Ni^{IV}(dtc)_3]^+$ as seen in **Figure 1.10** and **Equation 4**. The chemical step involves additional $Ni^{II}(dtc)_2$ molecules to facilitate the exchange of a dtc^- ligand. The undercoordinated Ni^{II} product is likely stabilized by solvent molecules, as the $Ni^{IV/II}$ oxidative wave is not observed in non-coordinating solvents.

$$3Ni^{II}(dtc)_2 \rightarrow 2[Ni^{IV}(dtc)_3]^+ + Ni^{II} + 4e^- \quad (4)$$

$$2[Ni^{IV}(dtc)_3]^+ + 2e^- \rightarrow 2Ni^{III}(dtc)_3) \quad (5)$$

$$2Ni^{III}(dtc)_3 + Ni^{II} + 2e^- \rightarrow 3Ni^{II}(dtc)_2 \quad (6)$$

Instead of a reversible $Ni^{IV/II}$ wave on the corresponding reduction, sequential, $1e^-$ reductions are observed. These correspond to the $1e^-$ reduction of $[Ni^{IV}(dtc)_3]^+$ to $Ni^{III}(dtc)_3$ (**Equation 5**) and an EC reaction where $Ni^{III}(dtc)_3$ reacts with the free Ni^{II} ion to yield $Ni^{II}(dtc)_2$ (**Equation 6**). This redox cycle demonstrates that while none of the waves are *reversible* in the traditional sense (*reversibility* will be defined in the next section), the redox cycle as a whole is reproducible, with stable Ni^{II} and Ni^{IV} species at the extreme potentials. The specific details of this redox cycle will be explored more in Chapter 2.

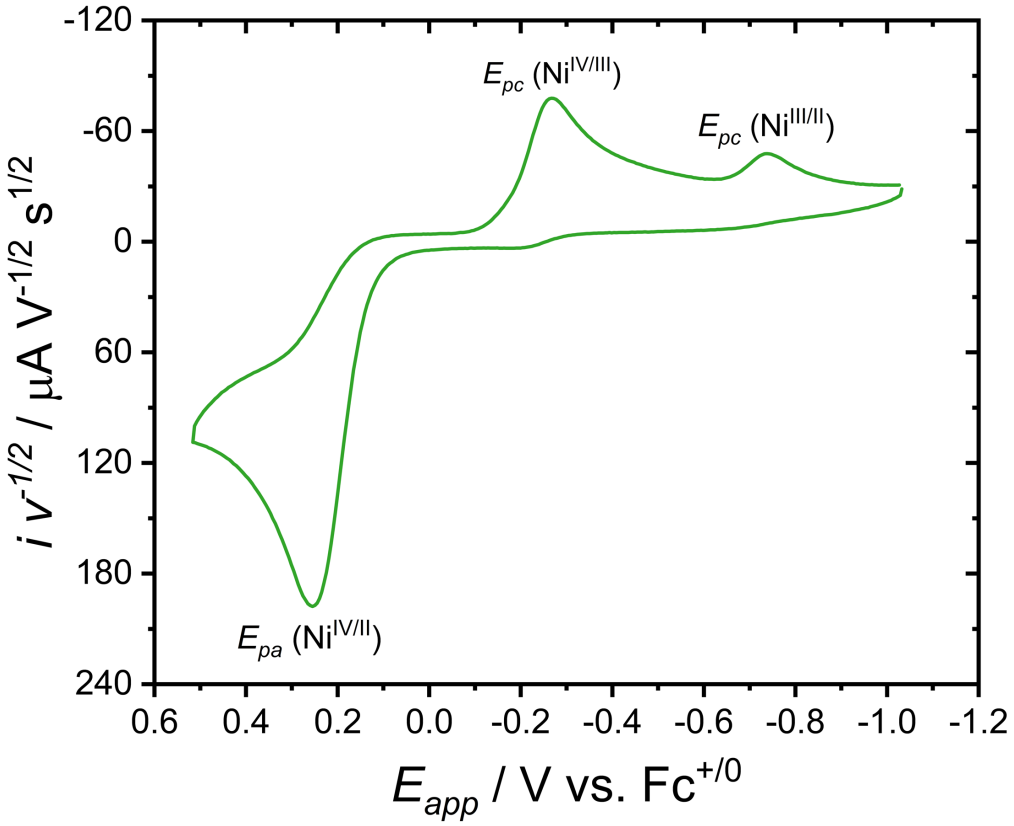

Figure 1.10. CV of 1 mM $Ni^{II}(dtc)_2$ in MeCN, 0.1 V/s, 0.1 M $TBAPF_6$, Glassy Carbon (GC) working electrode

Cyclic Voltammetry

Cyclic Voltammetry is a foundational electrochemical experiment, especially to chemists interested in electron transfer reactions of redox systems involving small, inorganic molecules. CVs become increasingly complex for multi-electron, EC/ECE processes, therefore, a brief background of the experimental technique is provided. In a CV, the x-axis corresponds to the potential (*E*) applied out of a working electrode (vs. a reference electrode), and the y-axis is the current (*i*) that is passed as a result of both oxidizing or reducing molecules in the solution (faradaic current) and double layer capacitance (non-faradic current). Like other electrochemical experiments, CV experiments require a supporting salt to be dissolved in solution to help conduct charge and decrease the thickness of the double-layer. A sample CV trace for the ferrocene/ferrocenium redox couple can be seen in **Figure 1.11**.[42]

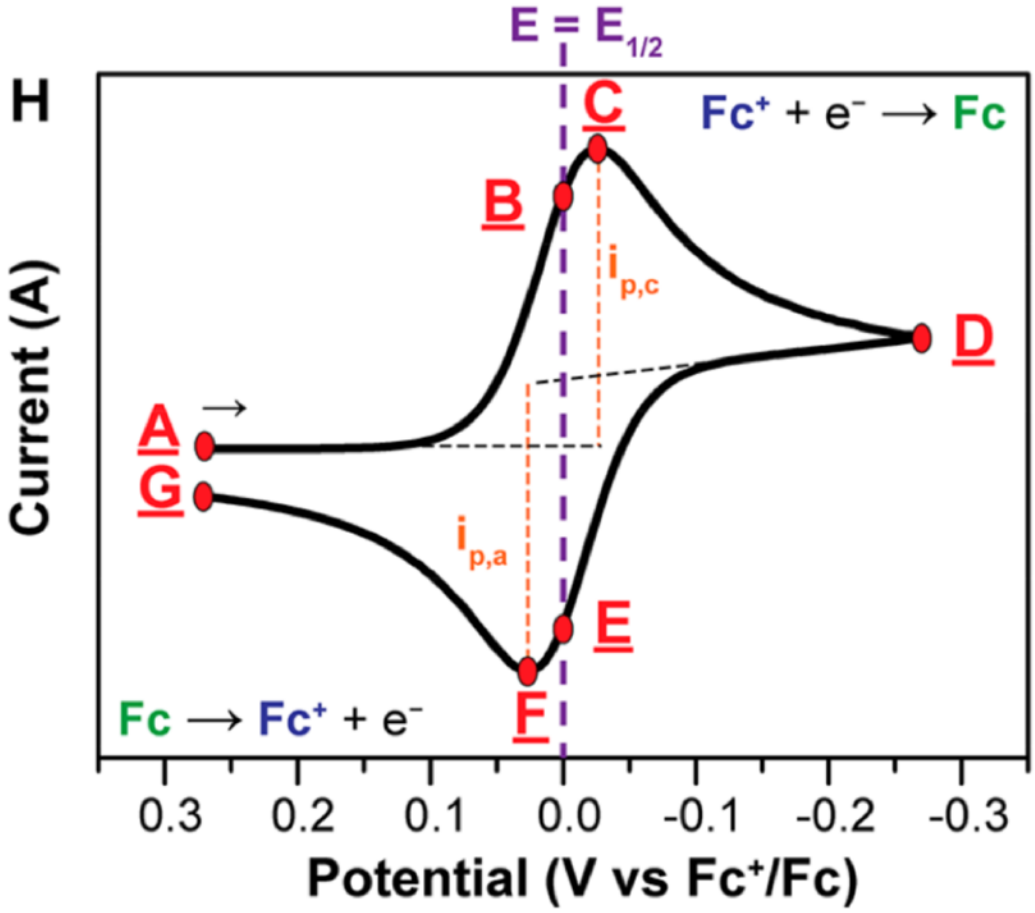

Figure 1.11. Sample cyclic voltammogram. Figure reprinted from Dempsey *et al*.[42]

In a CV experiment, the applied potential is swept linearly in a given direction at a set scan rate. Typically, this value is between 0.01 V/s and 10 V/s. The reversible ferrocene redox system seen in **Figure 1.11** provides a nice example of a cyclic voltammogram. A $1e^-$ redox couple is deemed electrochemically *reversible* when the difference in potential between E_{pa}, the anodic peak potential (point "F"), and E_{pc}, the cathodic peak potential (point "C"), is 59 mV. The peaks in a cyclic voltammogram are observed when the diffusion limit of the molecules to the surface of the electrode is achieved. In addition, the ratio of the anodic peak current (i_{pa}) to the cathodic peak current (i_{pc}) is 1. A *quasireversible* redox couple is one that loosely fits the expected peak splitting and current ratio for a reversible system; more will be said about quasireversible systems at the end of the section. In **Figure 1.11**, the ferrocenium ion (Fc^+) is reversibly reduced to ferrocene

(Fc) at 0.0 V vs. its own reduction potential, $E_{1/2}$ (potentials to follow are also vs. Fc^+/Fc). The $E_{1/2}$ for any given reaction is defined by **Equation 7** and related to the standard reduction potential, E^o, by **Equation 8**, where D_R is the diffusion coefficient for the reduced species and D_O is the diffusion coefficient for the oxidized species.

$$E_{1/2} = \frac{E_{pa}+E_{pc}}{2} \quad (7)$$

$$E_{1/2} = E^o - \frac{RT}{nF}\ln\left(\frac{D_R}{D_O}\right) \quad (8)$$

The $Fc^{+/0}$ redox couple can be observed at any of the scan rates listed above in a solvent such as MeCN. To observe the reduction from Fc^+ to Fc (at 0.0 V), the initial potential is set as 0.3 V at point "A", the switching potential is set as -0.3 V at point "D", and the final potential is set at 0.3 V at point "G". If the scan rate is 0.1 V/s, the potential decreases from 0.3 V to -0.3 V in six seconds. Upon reaching -0.3 V, the switching potential, the system then scans from -0.3 V back to 0.3 V at the same scan rate, thus taking six more seconds. This is where the "cyclic" term comes from: the potential is cycled from the initial, to the switching, and then the final potential (which is usually the same as the initial). This represents one full cycle completed.

At the reduction potential of $Fc^{+/0}$, faradaic current is passed as electrons are transferred into or out of the electrode, which is oxidation and reduction of the molecules, respectfully. The sign of the current is rather arbitrary and depends on the convention being used (IUPAC or U.S.), but the magnitude of the current in a CV, i_p, for an electrochemically reversible redox couple with freely diffusing molecules is determined by the Randles-Sevcik equation (**Equation 9**). Here, n is the number of electrons transferred, A is the area of the electrode (cm^2), C^0 is the bulk concentration

of the analyte (mol cm^{-3}), v is the scan rate (V s^{-1}), and D is the diffusion coefficient of the analyte (cm^2 s^{-1}):

$$i_p = 0.446nFAC^o\left(\frac{nFvD}{RT}\right)^{\frac{1}{2}} \quad (9)$$

Though the peak current, i_p, (y-axis) is determined by the variables in **Equation 9**, the peak potentials for an electrochemically reversible electron transfer process, E_{pa} and E_{pc}, (x-axis) are determined by **Equations 10 - 11**,[43] where α is the unitless transfer coefficient and k_s is the standard rate constant for electron transfer with the electrode surface (cm s^{-1}):

$$E_{pa} = E^0 + 0.78\frac{RT}{\alpha F} - \frac{RT}{(1-\alpha)F}\ln\left(k_s\sqrt{\left(\frac{RT}{(1-\alpha)FvD}\right)}\right) \quad (10)$$

$$E_{pc} = E^0 - 0.78\frac{RT}{\alpha F} + \frac{RT}{\alpha F}\ln\left(k_s\sqrt{\left(\frac{RT}{\alpha FvD}\right)}\right) \quad (11)$$

Using **Equations 10-11**, plots of peak potentials versus log(v) may be used to extract kinetic information such as k_s and α. In practice, if k_s is large, the natural logarithm term is insignificant over a wide range of scan rates and the peak position is constant, E_p - E^o = ±0.78(RT/αF). This condition is considered *reversible* electron transfer. However, when k_s is small, E_{pa} and E_{pc} shift by a factor of 59 mV per order of magnitude change in scan rate and the electron transfer is considered *quasireversible*. The typical "duck-like" shape seen in the CV of a reversible, $1e^-$ transfer reaction can be lost if a more complex mechanism is at hand (i.e. chemical reactions coupled with electron transfer [CE, EC] or multielectron processes [EE, ECE]). These concepts will be explored in the next section.

CVs with EC, CE, and EE Mechanisms

Figure 1.12 is a great visual representation of a few key concepts that will be explored more in the nickel dithiocarbamate redox cycle in Chapter 2. The CVs in **Figure 1.12** are all normalized to the square root of the scan rate ($v^{1/2}$). All scans proceed from negative potentials (left) to positive potentials (right), thus oxidizing molecules on the initial scan and reducing molecules on the return scan.

The first series of CVs are labeled "E_rC_i," meaning a reversible electron-transfer step occurs followed by an irreversible chemical step. This mechanism is represented by **Equations 12-13**:

Electron Transfer $\quad A \pm e^- \leftrightarrows B \quad (12)$

Chemical Reaction $\quad B \xrightarrow{k_f} C \quad (13)$

The scan performed at the fastest rate restores reversibility to the redox couple, as seen in the purple trace. This occurs because molecule "B" that is oxidized at the electrode is able to then be reversibly reduced back to "A" on the return scan before the irreversible chemical reaction step to "C" takes place. But if the forward rate constant for the C_i step, k_f, is fast enough, or if v is slow enough, E_{pc} will be observed but E_{pa} will not; the "duck-like" shape is lost (red trace).

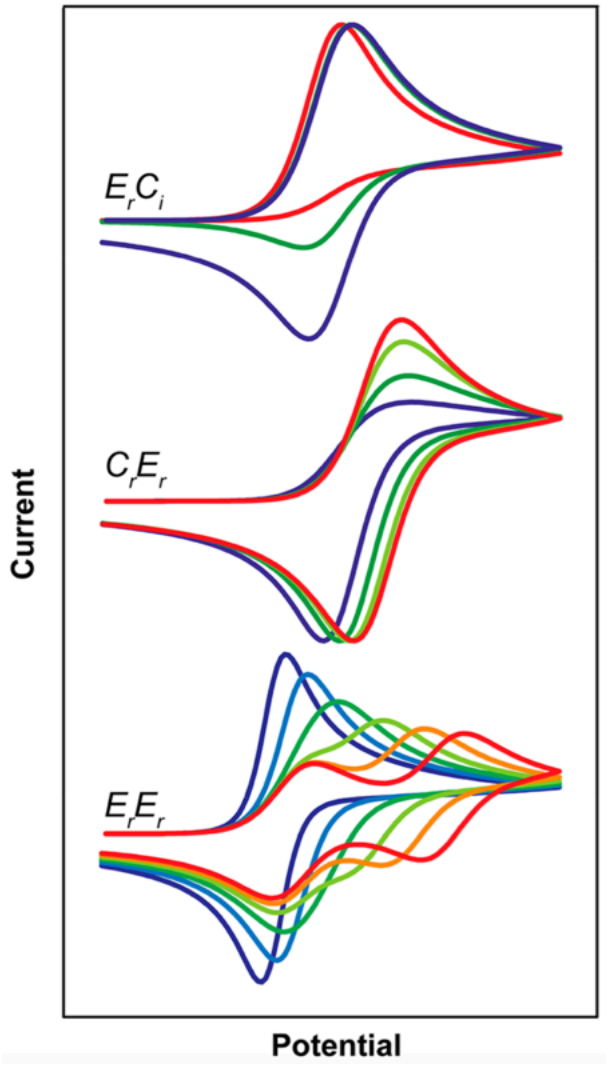

Figure 1.12. CVs modeled on DigiElch software. Figure reprinted from Dempsey *et al*.[42]

The second series of CVs seen in **Figure 1.12** are labeled "C_rE_r," meaning a reversible chemical reaction occurs followed by a reversible electron-transfer step. This mechanism is represented by **Equations 14-15**:

Chemical Reaction $\quad A \overset{k_f}{\leftrightarrows} B \quad (14)$

Electron Transfer $\quad B \pm e^- \leftrightarrows C \quad (15)$

In these CVs, v is held constant and k_f for the C_r step is increased. At small k_f (purple), E_{pc} is observed but E_{pa} is not observed due to the C_r step not producing a substantial amount of product "B" that can be oxidized to "C" on the timescale of the scan rate. However, at a large enough k_f (red), reversibility is observed, as both E_{pa} and E_{pc} are seen due to C_r producing a sufficient amount of "B" molecules capable of being oxidized to "C."

The third and final series of CVs in **Figure 1.12** are labeled "E_rE_r," meaning there are two, reversible $1e^-$ transfer steps. This mechanism is represented by **Equations 16-17**:

Electron Transfer $\quad A \pm e^- \leftrightarrows B \quad (16)$

Electron Transfer $\quad B \pm e^- \leftrightarrows C \quad (17)$

A regular, "duck-like" CV is shown in purple; this CV represents a single, $2e^-$ wave because the reduction potential for the second electron transfer (**Equation 17**) has been moved more negative than the reduction potential for the first electron transfer (**Equation 16**). However, as the reduction potential for the second electron transfer (**Equation 17**) is moved in the positive direction, two, $1e^-$ waves become increasingly resolved to the point where two sets of distinct peaks can be seen (red).

Each of the described mechanisms (EC, CE, EE) have their own derivations of **Equations 9-11**. However, since an ECE mechanism is observed in the nickel dithiocarbamate redox cycle, these concepts and principles learned from EC, CE, and EE mechanisms will be carried forth to understand the ECE mechanism.

CVs and the RSD-ECE Mechanism

In the nickel dithiocarbamate redox cycle, the concepts of combining E and C steps are taken a step further since the oxidation of $Ni^{II}(dtc)_2$ to $[Ni^{IV}(dtc)_3]^+$ occurs via an ECE mechanism. In particular, this oxidation is shown in Chapter 2 to occur through a Radical Substrate Dimerization (RSD) ECE mechanism, meaning that the chemical step involves a second substrate molecule which reacts with the newly generated electron transfer intermediate. This process is seen in **Equations 18-20** for general reactants:

Electron Transfer $\quad A \pm e^- \leftrightarrows B \quad (18)$

Chemical Reaction $\quad B + A \underset{k_{-c}}{\overset{k_c}{\leftrightarrows}} C \quad (19)$

Electron Transfer $\quad C \pm e^- \leftrightarrows D \quad (20)$

Since there are two, $1e^-$ transfer reactions in an ECE mechanism, the peak current, i_p, is expected to increase relative to the electrochemically reversible $1e^-$ transfer case. **Equation 9** is derived to yield **Equation 21** for peak current in the ECE case, which is valid at slow scan rates or fast chemical steps:

$$i_p = 0.992FAC^0\left(\frac{DFv}{RT}\right)^{\frac{1}{2}} \quad (21)$$

When CVs are normalized to $v^{1/2}$, it is found that the magnitude of i_p is greatest at the slow scan rate or large k_c conditions. The peak current is greatest for slow scan rates because the chemical reaction step (**Equation 19**) is given more time to occur, thus increasing the concentration of "C" which is able to undergo the second electron transfer to be reduced to "D" (as observed in **Equation 20**). Likewise, i_p is greatest for large k_c where the concentration of "C"

builds up quickly and is then able to undergo the second electron transfer step to be reduced to "D."

Equations 10-11, corresponding to E_{pa} and E_{pc} for a *quasireversible* one-electron transfer case, can be rewritten as **Equations 22 and 23** for the RSD-ECE mechanism.[43] Here, k_c is the rate constant (s^{-1}) for the chemical step associated with radical substrate dimerization.

$$E_{pa} = E^0 - 1.15\frac{RT}{F} + \frac{RT}{2F}\ln\left(\frac{4RT}{F}\frac{k_c C^0}{v}\right) \quad (22)$$

$$E_{pc} = E^0 + 1.15\frac{RT}{F} + \frac{RT}{2F}\ln\left(\frac{4RT}{F}\frac{k_c C^0}{v}\right) \quad (23)$$

In an RSD-ECE mechanism, the peak potential, E_p, shifts as a function of scan rate. As scan rate is decreased, E_{pa} shifts negatively. This observation can be explained through a Nernstian lens: the concentration of species "B" is able to build up over time and effectively increase the dimerization rate, as seen in **Equation 24**.

$$\text{Rate} = k_c[\text{A}][\text{B}] \quad (24)$$

Conclusion

The main objective of this work is to gain a better understanding of fundamental nickel chemistry and what conditions enable the unique redox cycle of nickel dithiocarbamates and cause these complexes to undergo $1e^-$ or $2e^-$ transfer reactions. The concepts and equations described in this chapter will be used throughout Chapter 2. The addition of an ancillary ligand, pyridine, to the electrochemical system enables reversibility in the primary redox event and we seek to understand the role this ancillary ligand plays in stabilizing a Ni^{III} intermediate. This knowledge can provide valuable insight for the design of nickel molecules for application in the field of energy storage.

Chapter Two: Influence of Pyridine on the Unique Multi-Electron Redox Cycle of Nickel Diethylthiocarbamate

Introduction

In Chapter 1, nickel dithiocarbamates were introduced and their noteworthy abilities explained. A background was also given on $2e^-$ chemistry, cyclic voltammetry, complex mechanisms, and potential application for $Ni^{II}(dtc)_2$ in RFBs. In this section, major points will be reexamined in light of $Ni^{II}(dtc)_2$ and the research reported within later sections of this chapter.

The world energy demand is expected to be 30 TW by the year 2050, more than double the world energy consumption of 13 TW in 2005.[44] In order to meet this demand, developments in technology to both harvest and store renewable energy are needed. A viable answer to energy storage is storing energy in the form of chemical bonds within the larger framework of a RFB. While there are examples of large-scale, commercially available RFBs,[6,45] further developments in terms of cost-efficiency and energy-density are needed long-term to ensure effective, widespread application of this technology. Namely, strategies focused on increasing the solubility of the active species, electrons transferred per molecule, potential difference in redox couples, long-term stability, and use of inexpensive anolytes and catholytes are needed. $Ni^{II}(dtc)_2$ directly contributes to four of these five areas: it has a $2e^-$ oxidation at a positive potential, can be cycled >100 times with little degradation, and has an earth-abundant first-row transition metal as the center of redox activity.

Moreover, few examples of stable, Ni^{IV} species exist, yet $Ni^{II}(dtc)_2$ can be easily oxidized to form stable, six-coordinate Ni^{IV} species. This transformation can be observed electrochemically and occurs via an ECE-RSD mechanism discussed later in this chapter. While this transformation undoubtably occurs through formation of a short-lived intermediate, it has not been detected.

However, with the addition of pyridine as an ancillary ligand, the primary redox event becomes reversible and the formation of a Ni^{III} intermediate is detected. These findings provide insight into the conditions that drive $2e^-$ transfer in this system and guide future design and development of MCCs for use in RFBs.

Experimental

General Considerations

All ^1H NMR spectra were recorded at room temperature at 600 MHz and used acetonitrile-d3 (Cambridge Isotope Laboratories, D, 99.8%) solvent. Peaks were calibrated from residual undeuterated solvent as an internal reference and chemical shifts are reported in parts per million (ppm) relative to tetramethylsilane (TMS). Abbreviations used in the NMR data: t, triplet; q, quartet. All other experiments were performed in acetonitrile (VWR Chemicals, HPLC Grade). Pyridine (Sigma-Aldrich, anhydrous 99.8%) and bromine (Alfa Aesar, 99.8%) were used as mentioned. Acetylferrocenium ($AcFc^+$) was synthesized according to previous reports.[46]

Synthesis and Characterization of $Ni^{II}(dtc)_2$

Nickel diethyldithiocarbamate $Ni^{II}(dtc)_2$ was prepared as previously described.[40] Two equivalents of sodium diethyldithiocarbamate trihydrate (Sigma, >99.0%) were added to one equivalent of nickel(II) chloride hexahydrate (Alfa Aesar, 98%) dissolved in distilled water. A green solid precipitated immediately and was filtered over vacuum and washed with cold distilled water, ethanol, and ether with 96% yield. Characterization of the light green solid by UV-Vis spectroscopy (**Figure S1**), ^1H NMR (**Figure S2**), and X-ray crystallography were consistent with a square planar, diamagnetic complex with bidentate coordination of dtc^- ligands. $Ni^{II}(dtc)_2$ was Electron Paramagnetic Resonance (EPR) silent (**Figure S3**), as expected for a d^8 metal center in a square planar environment.

Electrochemical Methods

Tetrabutylammonium hexafluorophosphate ($TBAPF_6$, Sigma-Aldrich, 98%) was recrystallized in absolute ethanol then dried over vacuum and stored in a desiccator. All cyclic voltammetry experiments used recrystallized $TBAPF_6$ to make 0.1 M $TBAPF_6$ MeCN electrolyte and were performed in a nitrogen environment. Spectroelectrochemical experiments used lithium bis(trifluoromethane)sulfonimide (LiTFSI, Sigma, 99.95%) to make 0.1 M LiTFSI MeCN electrolyte. The standard reduction potential of ferrocene (Alfa Aesar, 99%) was recorded before and after all electrochemical experiments to confirm consistency in reference electrode potentials. All potentials are reported versus the $Fc^{+/0}$ couple at 0 V. CV experiments were performed at room temperature on a WaveDriver 20 Bipotentiostat (Pine Research) with a glassy carbon disc working electrode (Pine Research, 5 mm diameter), Ag/Ag^+ non-aqueous reference electrode (BASi Instruments) with 0.001 M $AgNO_3$ in MeCN, and a platinum wire counter electrode. The glassy carbon working electrode was polished with 0.05 μm alumina powder (Allied High Tech Products Inc., DeAgglomerated). Cyclic voltammetry experiments were performed in a custom, smaller volume electrochemical cell modeled after the 150 mL Pine Research RDE/RRDE cell (solution dynamics were determined to be consistent with the original cell). All CVs were collected after compensating for the internal solution resistance. Spectroelectrochemical experiments were performed with the WaveDriver 20 Bipotentiostat. In this experimental setup, both the working and counter electrodes were on a platinum honeycomb electrode (Pine Research), and the reference electrode was a low-profile, Ag/Ag^+ non-aqueous electrode (Pine Research). $Ni^{II}(dtc)_2$ concentration in all electrochemical experiments was 1.0 mM.

Optical Measurements

UV-Vis spectra were collected on a Cary 8454 UV-Vis diode array system (Agilent). UV-Vis spectra obtained during spectroelectrochemical experiments were produced by an AvaLight-DHc light source (Avantes) and collected by an AvaSpec-2048 fiber optic spectrometer (Avantes).

EPR Methods

EPR tubes were frozen in liquid nitrogen. Continuous-wave EPR spectra were measured at X-band (9-GHz) frequency on a Bruker EMX spectrometer fitted with an ER-4119-HS (high-sensitivity) perpendicular-mode cavity. All measurements were collected at 77 K and performed by fitting the cavity with a liquid nitrogen finger Dewar. Spectra were recorded with a field modulation frequency of 100 kHz, modulation amplitude of 6.00 G, microwave power of 1.995 mW, and frequency of 9.370 GHz.

Electrochemical Modeling

DigiElch V8 from ElchSoft was used to model CV traces and produce a standard curve for the determination of k_{dec}.

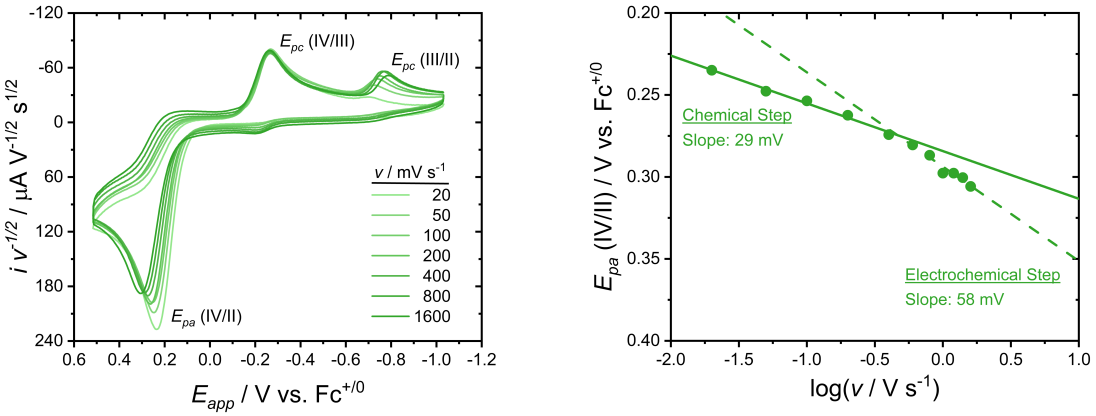

Figure 2.1. (a) CV data for 1 mM $Ni^{II}(dtc)_2$ in MeCN with 0.1 M $TBAPF_6$ electrolyte at room temperature. Current is shown normalized to scan rate (v) by dividing by $v^{1/2}$. Shifts in peak currents and peak potentials indicate the presence of redox reactions coupled to chemical steps in homogenous solution. (b) Anodic peak potential associated with $Ni^{IV/II}$ oxidation plotted versus log(v).

Results

Electrochemistry

Cyclic voltammetry (CV) experiments performed with $Ni^{II}(dtc)_2$ in acetonitrile (MeCN) solvent were consistent with those previously reported by Martin in acetone and Lachenal in acetonitrile.[40,41] **Figure 2.1a** shows CV data for 1 mM $Ni^{II}(dtc)_2$ as a function of scan rate (v) with current normalized to $v^{1/2}$. All data (**Tables S1-8**) were corrected for solution resistance and referenced to ferrocene ($Fc^{+/0}$). At v = 100 mV s^{-1}, an irreversible oxidation is observed at E_{pa} (IV/II) = 0.27 V assigned to the oxidation of four-coordinate $Ni^{II}(dtc)_2$ to six-coordinate $[Ni^{IV}(dtc)_3]^+$ via **Equation 1**. The stoichiometry of this reaction is complex due to the ligand exchange reaction that must occur in order to yield six-coordinate $[Ni^{IV}(dtc)_3]^+$. A total balance of this reaction to yield an uncoordinated (or solvent coordinated) Ni^{II} ion results in an overall number of electrons transferred per $Ni^{II}(dtc)_2$ molecule of n = 4/3, despite Ni^{II} being oxidized by 2e$^-$ to Ni^{IV}. Controlled potential electrolysis by Lachenal has confirmed this stoichiometry.[41] Subsequent reduction of $[Ni^{IV}(dtc)_3]^+$ back to $Ni^{II}(dtc)_2$ occurs through two irreversible reductions at E_{pc}

(IV/III) = -0.27 and E_{pc} (III/II) = -0.74 V via **Equation 2** and **Equation 3**, respectively. Although all three redox waves are electrochemically irreversible, the entire cycle is reproducible and always regenerates $Ni^{II}(dtc)_2$. For example, CV data collected at 100 mV s^{-1} showed only a 1.8% loss in current after 100 cycles (**Figure S4**).

(1) $3Ni^{II}(dtc)_2 \rightleftharpoons 2[Ni^{IV}(dtc)_3]^+ + Ni^{II} + 4e^-$

(2) $2[Ni^{IV}(dtc)_3]^+ + 2e^- \rightleftharpoons 2Ni^{III}(dtc)_3$

(3) $2Ni^{III}(dtc)_3 + Ni^{II} + 2e^- \rightleftharpoons 3Ni^{II}(dtc)_2$

The scan rate dependence of $Ni^{II}(dtc)_2$ oxidation (**Equation 1**) demonstrates that E_{pa} (IV/II) shifts positive with increasing scan rates. **Figure 2.1b** shows that at low scan rates, E_{pa} (IV/II) vs log(v) shows a linear dependence with a slope of 29 mV dec^{-1} while at high scan rates, the data are linear with a slope of 58 mV dec^{-1}. This behavior is consistent with an ECE/DISP mechanism for oxidation of Ni^{II} to Ni^{IV} described by **Equations 4-7**.[41] Here, E stands for an electrochemical step at the electrode surface, C stands for a chemical reaction step in homogenous solution, and DISP refers to an inherent disproportionation reaction which is competitive with the second E step. The chemical step specifically is proposed to involve ligand exchange between $[Ni^{III}(dtc)_2]^+$ and $Ni^{II}(dtc)_2$ to produce $Ni^{III}(dtc)_3$ and $[Ni^{II}(dtc)]^+$. Decomposition of $[Ni^{II}(dtc)]^+$ by **Equation 8** serves to satisfy the overall stoichiometry of **Equation 1**. Due to the fact that the chemical step consumes a second $Ni^{II}(dtc)_2$ molecule, this mechanism is specifically referred to as a radical substrate dimerization (RSD-ECE/DISP) and is often observed for the electrochemistry of halides, sulfides, organic radicals, and some organometallic species.[43,47-49]

(4) $Ni^{II}(dtc)_2 \rightleftharpoons [Ni^{III}(dtc)_2]^+ + e^-$ E

(5) $[Ni^{III}(dtc)_2]^+ + Ni^{II}(dtc)_2 \rightleftharpoons Ni^{III}(dtc)_3 + [Ni^{II}(dtc)]^+$ C

(6) $Ni^{III}(dtc)_3 \rightleftharpoons [Ni^{IV}(dtc)_3]^+ + e^-$ E

(7) $[Ni^{III}(dtc)_2]^+ + Ni^{III}(dtc)_3 \rightleftharpoons Ni^{II}(dtc)_2 + [Ni^{IV}(dtc)_3]^+$ DISP

(8) $2[Ni^{II}(dtc)]^+ \rightleftharpoons Ni^{II}(dtc)_2 + Ni^{II}$

The slope of 58 mV dec^{-1} at high scan rates indicates that E_{pa} (IV/II) is controlled by the quasireversible electron transfer kinetics associated with oxidation of $Ni^{II}(dtc)_2$ to four-coordinate $[Ni^{III}(dtc)_2]^+$ (**Equation 4**). The slope of 29 mV dec^{-1} at low scan rates indicates that the kinetics describing the ligand exchange reaction shown in **Equation 5** are exhibiting chemical control over the magnitude of E_{pa} (IV/II). In this regime, the scan rate is slow enough to allow for the chemical step to proceed appreciably and thus control the concentration of $[Ni^{III}(dtc)_2]^+$ at the electrode surface. The second electron transfer step needed to oxidize $Ni^{III}(dtc)_3$ to $[Ni^{IV}(dtc)_3]^+$ (**Equation 6**) or disproportionation reaction (**Equation 7**) has no bearing on E_{pa} (IV/II), however, they do influence the peak current, i_{pa} (IV/II).[43,47] As shown in **Figure S5**, i_{pa} (IV/II) $v^{-1/2}$ increases for low scan rates due to the ability for the chemical step to sufficiently produce $Ni^{III}(dtc)_3$ and thus allow for further oxidation. At appreciably fast scan rates, reduction of $[Ni^{III}(dtc)_2]^+$ at the electrode surface occurs faster than ligand exchange and the current stabilizes at a value consistent with $1e^-$ transfer via **Equation 4**.

The rate constants for **Equations 4-5** can be extracted from the scan rate dependence of E_{pa} (IV/II) using **Equations 8-9**, respectively. Here, E^o is the standard reduction potential for the $[Ni^{III}(dtc)_2]^+/Ni^{II}(dtc)_2$ redox couple, R is the ideal gas constant, T is temperature (298 K), F is Faraday's constant, n is the number of electrons transferred in **Equation 4** ($n = 1$), α is the electron transfer exchange coefficient, and λ is the unitless kinetic parameter associated with each step. For a chemically controlled step, $\lambda_c = k_c RT/nFv$, where k_c is the pseudo first-order rate constant (s^{-1}) for the chemical step. For an electrochemically controlled step, $\lambda_E = k_E^2 RT/\alpha nFDv$, where k_E is the

rate constant for electron transfer at the electrode surface (cm s^{-1}) and D is the diffusion coefficient (cm^2 s^{-1}). The standard reduction potential for the $[Ni^{III}(dtc)_2]^+/Ni^{II}(dtc)_2$ redox couple was estimated to be E^o = 0.25 V based on data collected between 4 and 40 V s^{-1} (**Figure S6**) where reduction of $[Ni^{III}(dtc)_2]^+$ could be observed. Extrapolation of the low scan rate data in **Figure 2.1b** to the condition of log(v) = 0 allowed for k_c = 34 s^{-1} to be estimated. Taking the general assumption that D = 10^{-5} cm^2 s^{-1}, extrapolation of high scan rate data to log(v) = 0 yielded an estimate of α = 0.51 based on the slope of 58 mV dec^{-1} and k_E = 0.018 cm s^{-1} from on the intercept.[43,47,50]

(8) E_{pa} (IV/II) = E^o + 1.15(RT/nF) – (2.303RT/2nF)logλ_C

(9) E_{pa} (IV/II) = E^o + 1.15(RT/αnF) – (2.303RT/2αnF)logλ_E

Reduction of $[Ni^{IV}(dtc)_3]^+$ to $Ni^{III}(dtc)_3$ by **Equation 2** shows very little dependence on scan rate, indicating that the reduction occurs with a large electron transfer rate constant. **Figure S7** shows a plot of E_{pc} (IV/III) vs log(v) where E_{pc} (IV/III) remains between -0.26 and -0.27 V from 20 – 1600 mV s^{-1}. In contrast, reduction of $Ni^{III}(dtc)_3$ to $Ni^{II}(dtc)_2$ via **Equation 3** exhibits a clear dependence of E_{pc} (III/II) on scan rate, **Figure S8**. This dependence can be justified based on the EC mechanism shown in **Equations 10-11** which involves ligand exchange between $[Ni^{II}(dtc)_3]^-$ and Ni^{II} to regenerate $Ni^{II}(dtc)_2$.

(10) $Ni^{III}(dtc)_3 + e^- \rightarrow [Ni^{II}(dtc)_3]^-$

(11) $2[Ni^{II}(dtc)_3]^- + Ni^{II} \rightarrow 3Ni^{II}(dtc)_2$

The normalized peak current for $Ni^{III}(dtc)_3$ reduction (i_{pc} (III/II) $v^{-1/2}$) was also observed to increase prominently with faster scan rates (**Figure S5**). This behavior is consistent with a preceding chemical step which controls the concentration of $Ni^{III}(dtc)_3$ prior to reduction by **Equation 3**. We propose this step to be the redox disproportionation of $Ni^{III}(dtc)_3$ and $[Ni^{III}(dtc)_2]^+$

to yield $[Ni^{IV}(dtc)_3]^+$ and $Ni^{II}(dtc)_2$ describes by **Equation 7**. The formation of $[Ni^{III}(dtc)_2]^+$ is thought to occur by the reverse step of **Equation 5**, indicating this step must have a relatively small equilibrium constant.

Diethyldithiocarbamate Addition

Na(dtc) was added to MeCN solutions of $Ni^{II}(dtc)_2$ to study the impact on the ligand exchange reactions noted above. **Figure 2.2** shows voltammograms measured at 1 mM Na(dtc) and 1 mM $Ni^{II}(dtc)_2$ as a function of scan rate. At 100 mV s^{-1}, the irreversible oxidation of dtc^- to $dtc^\bullet$ in **Equation 12** can be observed at E_{pa} ($dtc^{\bullet/-}$) = -0.45 V, consistent with previous literature studies.[40] Furthermore, a dramatic increase in current associated with oxidation of $Ni^{III}(dtc)_3$ to $[Ni^{IV}(dtc)_3]^+$ can be observed at E_{pa} (IV/III) = -0.21 V. This increase in current can be described by a CE mechanism where chemical oxidation of $Ni^{II}(dtc)_2$ by $dtc^\bullet$ in homogenous solution (**Equation 13**) occurs prior to electrochemical oxidation to $[Ni^{IV}(dtc)_3]^+$. Interestingly, the peak potential and current for oxidation of $Ni^{II}(dtc)_2$ to $[Ni^{IV}(dtc)_3]^+$ is not greatly affected by larger $[dtc^-]$. This is believed to be the result of dtc^- depletion at the electrode surface due to oxidation and consumption at more negative potentials, thus leaving no significant concentration available to coordinate to the oxidized nickel center.

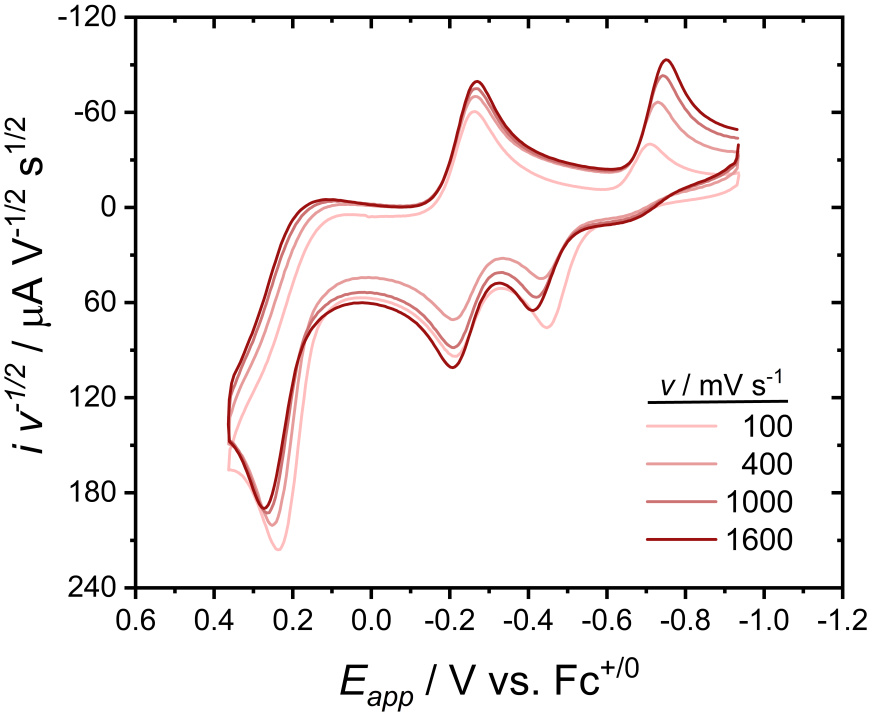

Figure 2.2. CV data for 1 mM $Ni^{II}(dtc)_2$, 1 mM Na[dtc] in MeCN with 0.1 M $TBAPF_6$ electrolyte at room temperature.

(12) $[dtc]^- \rightarrow dtc^\bullet + e^-$

(13) $Ni^{II}(dtc)_2 + dtc^\bullet \rightarrow Ni^{III}(dtc)_3$

Reduction of $Ni^{III}(dtc)_3$ to $Ni^{II}(dtc)_2$ exhibits a much larger scan rate dependence in the presence of excess dtc^- than in its absence. Much like the data shown in **Figure 2.1**, i_{pc} (III/II) increases with larger scan rates. However, in the presence of dtc^-, i_{pc} (III/II) increases to values equal to that of i_{pc} (IV/III). This indicates that the disproportionation reaction in **Equation 7**, which decreases the concentration of $Ni^{III}(dtc)_3$, is being suppressed in the presence of dtc^-. We propose that this observed behavior is due to coordination of dtc^- to Ni^{II}, thus preventing the formation of $[Ni^{III}(dtc)_2]^+$ by the reverse step of **Equation 5**.

Pyridine Addition

The ligand exchange reaction shown in **Equation 5** is clearly an important step in both oxidation of $Ni^{II}(dtc)_2$ and reduction of $Ni^{III}(dtc)_3$. The details of this reaction are not currently well understood and likely involve multiple individual steps to achieve the overall reaction. We surmise that solvent must play a role in stabilizing intermediate species such as $[Ni^{III}(dtc)_2]^+$, Ni^{II}, $[Ni^{II}(dtc)]^+$, or even dimer species needed to facilitate exchange of the dtc^- ligand. Thus, CV experiments were conducted for $Ni^{II}(dtc)_2$ dissolved in MeCN with controlled additions of pyridine to investigate the effect of a more strongly coordinating solvent ligand. **Figure 2.3a** shows CV data collected at 1000 mV s^{-1} for 1 mM $Ni^{II}(dtc)_2$ in MeCN over a range of [py] = 0 – 383 mM. The $Ni^{II}(dtc)_2$ oxidation peak was found to shift in a negative direction from 0.30 V to -0.02 V over this concentration range while the reversibility of the redox wave increased. The increase in reversibility of this shifted redox feature was concomitant with a noticeable loss in peak current associated with reduction of $[Ni^{IV}(dtc)_3]^+$ (i_{pc} (IV/III)). This could also be observed in the scan rate dependent normalized voltammograms shown in **Figure 2.3b** where the rise of the new cathodic peak near -0.1 V at higher scan rates occurs with a decrease in peak current for i_{pc} (IV/III) (**Figure S9**).

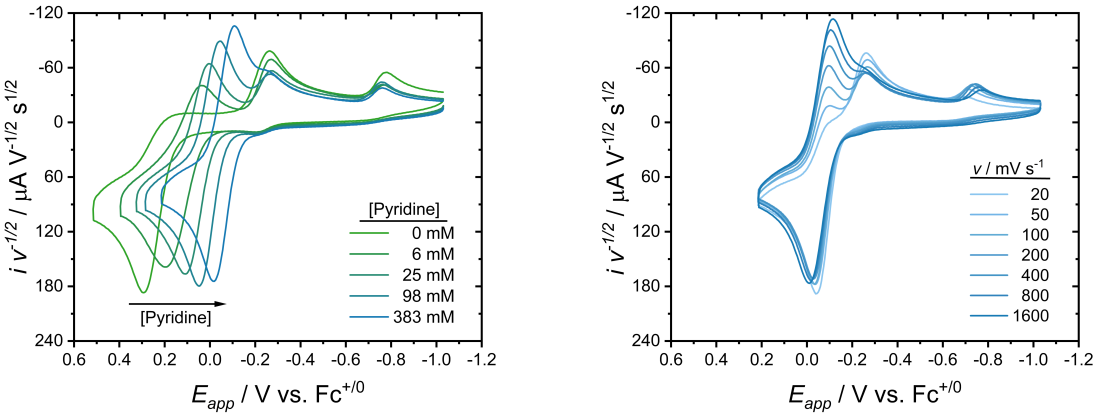

Figure 2.3. (a) CV data of 1 mM $Ni^{II}(dtc)_2$ in MeCN with added pyridine. All data collected with 0.1 M $TBAPF_6$ at room temperature. (b) CV data of 1 mM $Ni^{II}(dtc)_2$, 383 mM Py in MeCN. All data collected with 0.1 M $TBAPF_6$ at room temperature.

The peak splitting of the shifted redox wave was found to be $\Delta E_p = E_{pa} - E_{pc} = 62$ mV at 100 mV s^{-1} and 91 mV at 1000 mV s^{-1} (**Figure S10**), consistent with a quasireversible $1e^-$ transfer reaction. This new redox wave is therefore proposed to be the result of $Ni^{II}(dtc)_2$ oxidation to a pyridine coordinated $[Ni^{III}(dtc)_2(py)_2]^+$ species shown in **Equation 14**. EPR experiments confirmed the presence of Ni^{III} using acetylferrocenium as a chemical oxidant in the presence of pyridine (**Figure S3**). The $g_{avg} \sim 2.13$ was consistent with other reports of Ni^{III} species. However, the signal changed significantly with increased pyridine concentration.[51,52] Further experiments are currently underway to decipher this behavior and characterize the pyridine coordinated Ni^{III} structure. Notably, the EPR signal was only observed in the presence of oxidant and pyridine with oxidant only conditions yielding an EPR silent species believed to be low spin $[Ni^{IV}(dtc)_3]^+$.

(14) $Ni^{II}(dtc)_2 + 2py \rightarrow [Ni^{III}(dtc)_2(py)_2]^+ + e^-$

(15) $[Ni^{III}(dtc)_2]^+ + 2py \rightarrow [Ni^{III}(dtc)_2(py)_2]^+$

(16) $E_{1/2} = E^o - (RT/F)\ln(K')$

Equation 14 likely proceeds by an EC mechanism where $Ni^{II}(dtc)_2$ is first oxidized to $[Ni^{III}(dtc)_2]^+$ followed by addition of pyridine. This is reasoned based on ^1H NMR and UV-Vis evidence that suggests the equilibrium constant for pyridine coordination to $Ni^{II}(dtc)_2$ is immeasurably small (**Figures S2, S11**). The equilibrium constant for pyridine coordination to $[Ni^{III}(dtc)_2]^+$ (**Equation 15**) was determined using the shift in $E_{1/2}$ as a function of pyridine concentration according to **Equation 16**, where E^o = 0.25 V is the standard potential for the $[Ni^{III}(dtc)_2]^+/Ni^{II}(dtc)_2$ couple. A plot of K' vs [py] is shown in **Figure 2.4** where a clear second order dependence on pyridine can be observed, indicating that a six coordinate Ni^{III} species is produced. The equilibrium constant for the coordination of the two pyridine ligands was extracted with the quadratic fit, $K' = K[py]^2$. An average estimate of K = 1.2 (± 0.2) x 10^6 M^{-2} was obtained using data collected over a range in scan rates of 100 – 1600 mV s^{-1} (**Table S9**). Based on this equilibrium constant, an $E_{1/2}$ = -0.24 V would be expected in pure pyridine solvent ([py] = 12.4 M). Indeed, **Figure S12** shows CV data collected in pure pyridine where an $E_{1/2}$ = -0.28 V is experimentally measured, consistent with our calculated estimate.

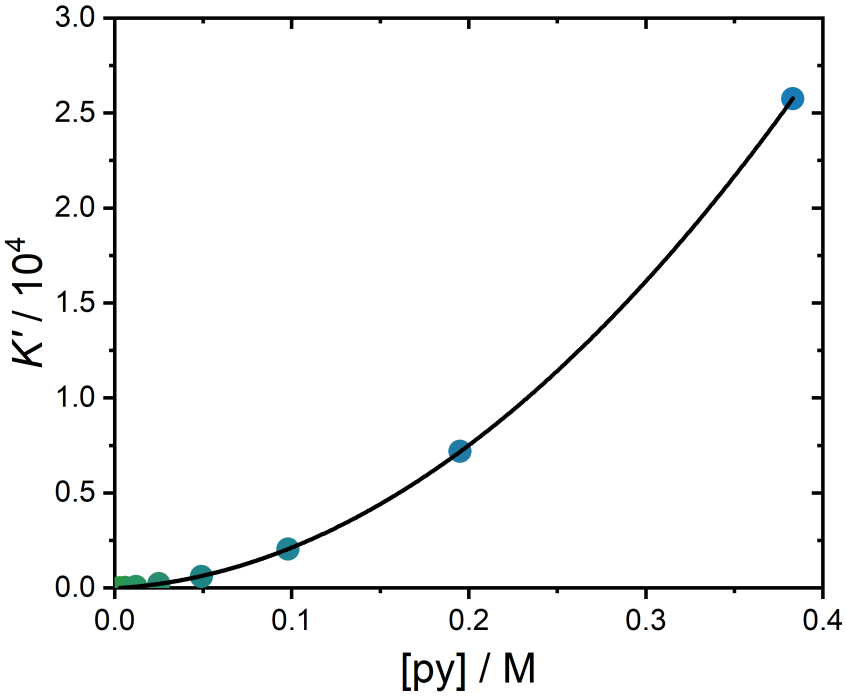

Figure 2.4. Determination of the equilibrium constant (K = 1.2 (± 0.2) x 10^6 M^{-2}) for pyridine coordination to $[Ni^{III}(dtc)_2]^+$ based on **Equations 15-16**. Data points represent v = 1000 mV s^{-1}.

The reversibility of the $[Ni^{III}(dtc)_2(py)_2]^+/Ni^{II}(dtc)_2$ redox wave is highly dependent on both [py] and scan rate. Quasireversibility is observed at large [py] and large v while irreversibility is observed at low [py] and low v. Plots of E_{pa} (III_{py}/II) vs log(v) also reflect these trends as shown in **Figures S13-14**. For [py] < 10 mM, a slope of ~30 mV dec^{-1} was observed, indicating a chemical step following electron transfer. For [py] > 10 mM, the slope decreased monotonically toward zero, indicating more reversible behavior.[53] These characteristics, coupled with the inverse dependence in cathodic peak currents between the $[Ni^{III}(dtc)_2(py)_2]^+/Ni^{II}(dtc)_2$ and $[Ni^{IV}(dtc)_3]^+/Ni^{III}(dtc)_3$ couples, suggest that irreversible decomposition of $[Ni^{III}(dtc)_2(py)_2]^+$ into $[Ni^{IV}(dtc)_3]^+$ must be occurring on the timescale of the CV experiment.

Evaluating the ratio of peak currents (i_{pc}/i_{pa}) as an indicator of the stability of $[Ni^{III}(dtc)_2(py)_2]^+$ allows determination of the rate constant for the decomposition reaction (k_{dec}).

A plot of i_{pc}/i_{pa} for the $[Ni^{III}(dtc)_2(py)_2]^+/Ni^{II}(dtc)_2$ wave versus log(v) is shown in **Figure 2.5a** where the decomposition rate constant is determined using a working curve for an ECE/DISP mechanism generated using DigiElch software. Values of k_{dec} over the range of pyridine concentrations are given in **Table 2.1**.

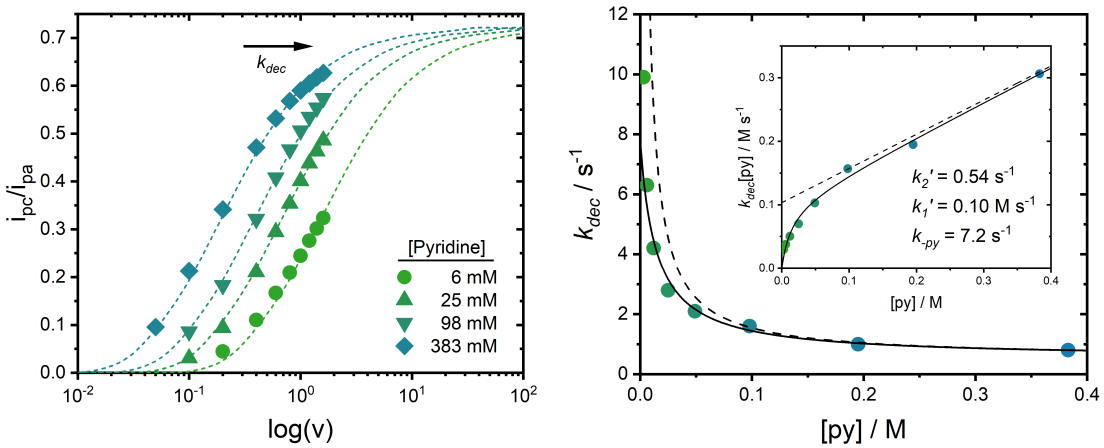

Figure 2.5. (a) Ratio of peak currents associated with the $Ni^{III}(dtc)_2(py)_2/Ni^{II}(dtc)_2$ redox couple plotted versus log(v). The decomposition rate constant (k_{dec}) was determined for each [py] using working curves (dashed lines) generated for a general ECE/DISP mechanism. (b) Plot of k_{dec} vs [py] showing a decreasing in k_{dec} for higher [py]. The solid overlaid line represents a fit to **Equation 20** with rate constants given in the figure. The dashed overlaid line represents the limiting form of **Equation 20** at high [py]. Inset shows a plot of k_{dec}[py] vs [py] to highlight the linear dependence at high [py]. Overlaid lines are the same as those of the main figure.

The decomposition rate constant is shown to decrease with higher [py], consistent with stabilization of the $[Ni^{III}(dtc)_2(py)_2]^+$ species. Furthermore, the inverse dependence on pyridine indicates that decomposition of $[Ni^{III}(dtc)_2(py)_2]^+$ to yield $[Ni^{IV}(dtc)_3]^+$ must involve an equilibrium reaction which dissociates pyridine from the nickel metal center. Therefore, we propose that the decomposition of $[Ni^{III}(dtc)_2(py)_2]^+$ occurs through two parallel reaction pathways: one in which ligand exchange with $Ni^{II}(dtc)_2$ via **Equation 17** occurs and another in which dissociation of a single pyridine to produce $[Ni^{III}(dtc)_2py]^+$ (**Equation 18**) which then undergoes ligand exchange with $Ni^{II}(dtc)_2$ via **Equation 19**. If a steady-state approximation is

made for the decay of $[Ni^{III}(dtc)_2py]^+$, then the parallel reaction scheme can be described by an overall k_{dec} given by **Equation 20**, where $k_2' = k_2[Ni^{II}(dtc)_2]_0$ and $k_1' = (k_1/K_{3,py2})[Ni^{II}(dtc)_2]_0$. The rate constants k_2 and k_1 describe the ligand exchange reactions for $[Ni^{III}(dtc)_2(py)_2]^+$ and $[Ni^{III}(dtc)_2py]^+$, respectively. The equilibrium constant $K_{3,py2} = k_{+py}/k_{-py}$ describes the association constant for the coordination of the second pyridine ligand to Ni^{III} shown in **Equation 18** with k_{+py} being the rate constant for pyridine coordination and k_{-py} being the rate constant for pyridine dissociation. A complete derivation of this expression is shown in the Supporting Information.

Table 2.1. Summary of $E_{1/2}$ and k_{dec} measured for the $Ni^{III}(dtc)_2(py)_2/Ni^{II}(dtc)_2$ redox couple as a function of pyridine concentration

[py] / mM	$E_{1/2}$ **/ V vs** $Fc^{+/0}$	k_{dec} **/** s^{-1}
0	-	-
3	0.14	9.9
6	0.12	6.3
12	0.09	4.2
25	0.06	2.8
49	0.03	2.1
98	0.00	1.6
195	-0.03	1.0
383	-0.06	0.8

(17) $[Ni^{III}(dtc)_2(py)_2]^+ + Ni^{II}(dtc)_2 \rightarrow Ni^{III}(dtc)_3 + [Ni^{II}(dtc)(py)_2]^+$

(18) $[Ni^{III}(dtc)_2(py)_2]^+ \rightleftharpoons [Ni^{III}(dtc)_2py]^+ + py$

(19) $[Ni^{III}(dtc)_2py]^+ + Ni^{II}(dtc)_2 \rightarrow Ni^{III}(dtc)_3 + [Ni^{II}(dtc)py]^+$

(20) $$k_{dec} = k_2[Ni^{II}(dtc)_2]_0 + \frac{k_1[Ni^{II}(dtc)_2]_0 k_{-py}}{k_1[Ni^{II}(dtc)_2]_0 + k_{+py}[py]} = k_2' + \frac{k_1' k_{-py}}{k_1' + k_{-py}[py]}$$

Analysis of k_{dec} as a function of [py] is shown in **Figure 2.5b** where the solid line represents a fit to **Equation 20**. The extracted rate constants are $k_2' = 0.54$ s^{-1}, $k_1' = 0.10$ M s^{-1}, and $k_{-py} = 7.2$ s^{-1}. Given that $[Ni^{II}(dtc)_2]_0 = 1$ mM, $k_2 = 540$ M^{-1} s^{-1} and $k_1/K_{3,py2} = 100$ s^{-1}. At high pyridine

concentration, **Equation 20** takes the limiting form $k_{dec} = k_2' + k_1'/[py]$. Multiplication by [py] allows for a linear expression to be obtained, $k_{dec}[py] = k_2'[py] + k_1'$. Fits to these limiting expressions (k_{dec} and $k_{dec}[py]$) are shown as dashed lines in **Figure 2.5b** with the inset plot highlighting the linear behavior at high [py]. As the pyridine concentration increases further, k_{dec} will asymptotically approach k_2', representative of decomposition only through the ligand exchange via **Equation 17**.

The reduction of $[Ni^{IV}(dtc)_3]^+$ and $Ni^{III}(dtc)_3$ were not significantly impacted by the presence of pyridine, as shown by the similar cathodic peak positions when compared to blank MeCN. **Figure S8** shows a comparison of E_{pc} (III/II) vs log(v) for 0 and 383 mM pyridine concentrations. The slope for both plots is 39 mV dec^{-1} indicating an EC mechanism as described by **Equations 10-11**. The exact nature of the chemical step may be different in the presence of pyridine due to coordination of Ni^{II} ions; however, this step was not explored further.

Spectroelectrochemistry

Spectroelectrochemistry of $Ni^{II}(dtc)_2$ in MeCN with and without pyridine were performed to investigate the possible detection of the $[Ni^{III}(dtc)_2(py)_2]^+$ intermediate. **Figure 2.6a** shows UV-visible absorption spectra of $Ni^{II}(dtc)_2$ collected as a function of applied potential in the absence of pyridine. At increasingly positive applied potentials, decay of the $Ni^{II}(dtc)_2$ absorbance spectrum with λ_{max} = 388 nm gives rise to a broad increase in absorbance across the visible region with λ_{max} = 445 nm, consistent with the formation of $[Ni^{IV}(dtc)_3]^+$. The absorbance spectrum of $[Ni^{IV}(dtc)_3]^+$ has been reported previously and these results are consistent with those performed by Martin in acetone solvent.[40] **Figure 2.6b** shows an identical experiment performed with [py] = 98 mM in which clean conversion from $Ni^{II}(dtc)_2$ to $[Ni^{IV}(dtc)_3]^+$ can be observed with no intermediate absorbance features. Conversion from $Ni^{II}(dtc)_2$ to $[Ni^{IV}(dtc)_3]^+$ occurred with $E_{1/2}$ =

0.10 V in the absence of pyridine and $E_{1/2}$ = -0.06 V in the presence of pyridine. This shift in $E_{1/2}$ was consistent with CV results discussed above. The ultimate formation of $[Ni^{IV}(dtc)_3]^+$ in the spectroelectrochemical experiments point to a mechanism in which pyridine is able to catalyze the formation of $[Ni^{IV}(dtc)_3]^+$ through the formation of a $[Ni^{III}(dtc)_2(py)_2]^+$ intermediate.

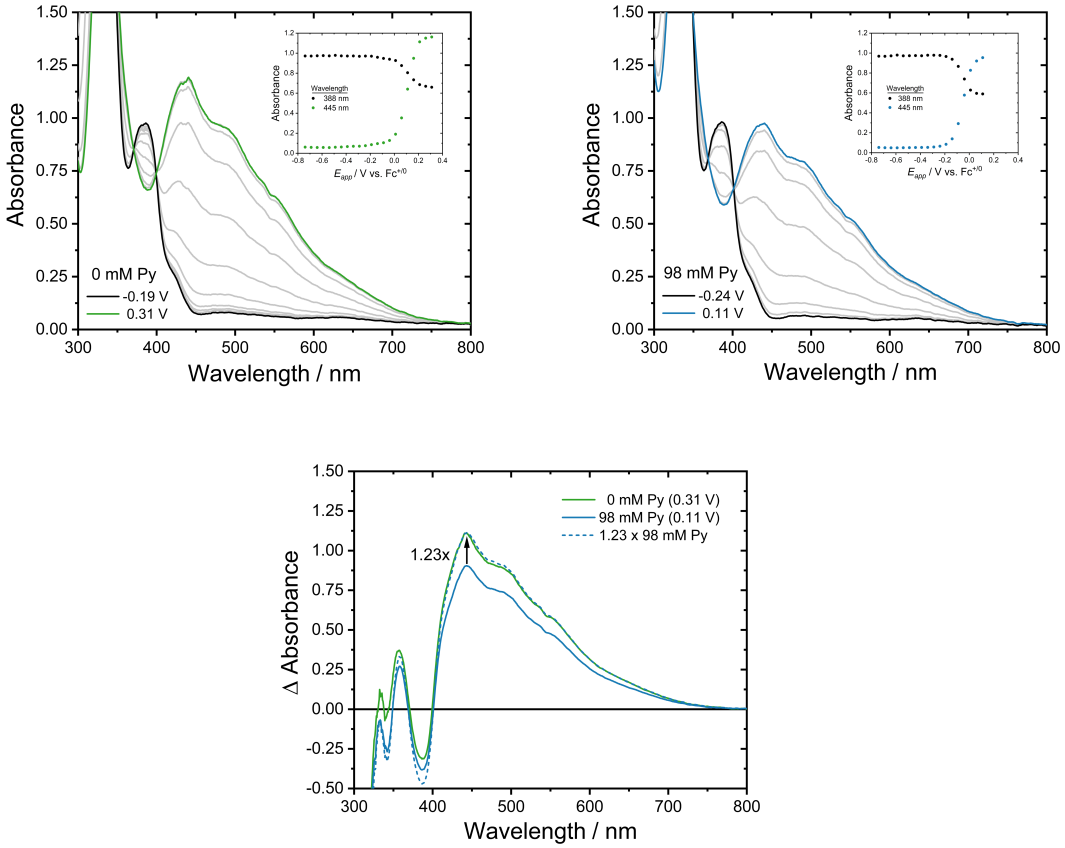

Figure 2.6. Spectroelectrochemical data collected for $Ni^{II}(dtc)_2$ with (a) [py] = 0 mM and (b) [py] = 98 mM. Conversion from $Ni^{II}(dtc)_2$ to $[Ni^{IV}(dtc)_3]^+$ can be observed cleanly in both cases with identical isosbestic points. (c) Comparison of final ΔAbs spectra collected at the condition of complete oxidation to $[Ni^{IV}(dtc)_3]^+$. The total yield of $[Ni^{IV}(dtc)_3]^+$ in the absence of pyridine was 1.23x larger than the total yield in the presence of pyridine.

Notably, the concentration of $[Ni^{IV}(dtc)_3]^+$ produced in the absence of pyridine was 1.23x larger than that produced in the presence of pyridine. **Figure 2.6c** shows the ΔAbs spectra recorded under complete oxidation conditions with and without pyridine along with a normalized

comparison to show the difference in magnitude. A decreased $[Ni^{IV}(dtc)_3]^+$ yield in the presence of pyridine similar in magnitude to the data in **Figure 6** was consistently observed over multiple experiments. This data shows that a change in stoichiometry must be occurring when pyridine is involved in the oxidation reaction. We believe this change is due to the ability of pyridine to stabilize undercoordinated Ni^{II} species that are formed as result of ligand exchange, thus producing $[Ni^{II}(dtc)(py)_2]^+$ as a product, **Equation 21**. In effect, this decreases the number of $[Ni^{IV}(dtc)_3]^+$ produced by preserving some Ni^{II}-dtc bonds.

(21) $2Ni^{II}(dtc)_2 + 2py \rightarrow [Ni^{IV}(dtc)_3]^+ + [Ni^{II}(dtc)(py)_2]^+ + 2e^-$

Oxidation in the presence of pyridine is contrasted to the case of pure acetonitrile solvent where free Ni^{II} ions are produced. It is likely these ions are still coordinated with MeCN in some way, however, MeCN is not a strong enough ligand to stabilize a $[Ni^{II}(dtc)(MeCN)_2]^+$ species. In the absence of pyridine, **Equation 1** describes the net oxidation reaction where the ratio of Ni^{IV} produced to Ni^{II} consumed is 2/3. In the presence of pyridine, this ratio decreases to 1/2 according to **Equation 21**. Therefore, the amount of $[Ni^{IV}(dtc)_3]^+$ produced in the absence of pyridine would be 1.3 times larger than the amount produced in the presence of pyridine, similar to the experimentally determined value of 1.23 shown in **Figure 2.6**.

Discussion

Oxidation/Reduction of $Ni^{II}(dtc)_2$ in the absence of pyridine

The multi-electron redox cycle of $Ni^{II}(dtc)_2$ in acetonitrile solvent can be described using the thermochemical cycle shown in **Scheme 2.1**. Horizontal arrows indicate $1e^-$ transfer reactions and vertical arrows describe equilibria of bis-chelated nickel complexes with $Ni^{II}(dtc)_2$ as stated for the general reaction in **Equation 22**. According to **Scheme 2.1**, oxidation of $Ni^{II}(dtc)_2$ to

$[Ni^{IV}(dtc)_3]^+$ must proceed through two 1e$^-$ transfer steps and one equilibrium. This may be achieved by three pathways: 1) sequential oxidation of $Ni^{II}(dtc)_2$ to $[Ni^{IV}(dtc)_2]^+$ followed by ligand exchange to $[Ni^{IV}(dtc)_3]^+$ (*i.e.* $E^o_1 \rightarrow E^o_2 \rightarrow K_4$); 2) ligand exchange to $[Ni^{II}(dtc)_3]^-$ followed by sequential oxidation (*i.e.* $K_2 \rightarrow E^o_3 \rightarrow E^o_4$); or 3) oxidation to $[Ni^{III}(dtc)_2]^+$ followed by ligand transfer to $Ni^{III}(dtc)_3$ and oxidation to $[Ni^{IV}(dtc)_3]^+$ (*i.e.* $E^o_1 \rightarrow K_3 \rightarrow E^o_4$). The ECE/DISP mechanism described by **Equation 4-7** constitutes pathway 3 and was originally proposed by Lachenal.[41]

The standard redox potential E^o_1 = 0.25 V was estimated here using CV data collected at high scan rates. The redox potentials of E^o_3 = -0.71 V and E^o_4 = -0.24 V were originally reported by Lachenal[41] and are consistent with the data presented here. The potential E^o_2 for the $[Ni^{IV}(dtc)_2]^{2+}/[Ni^{III}(dtc)_2]^+$ has not been previously reported and was not determined in the present study. Estimates of K_2, K_3, and K_4 are also not available in the literature, however, the difference in E^o_3 and E^o_1 can be used to estimate the ratio of equilibrium constants $K_3/K_2 = 1.7 \times 10^{16}$ based on the relation $(E^o_3 - E^o_1) = (RT/F)\ln(K_3/K_2)$.

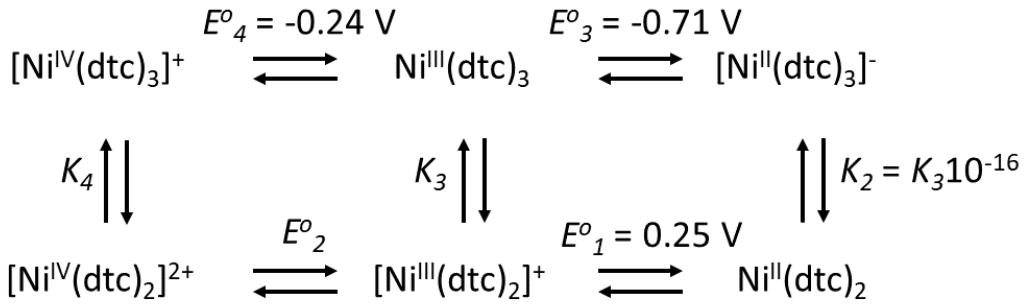

Scheme 2.1. Thermochemical cycle describing the multiple electron transfer and ligand transfer reactions involved in the $[Ni^{IV}(dtc)_3]^+/Ni^{II}(dtc)_2$ redox couple.

(22) $[Ni^z(dtc)_2]^{z-2} + Ni^{II}(dtc)_2 \rightleftharpoons [Ni^z(dtc)_3]^{z-3} + [Ni^{II}L]^+$ K_z

The scan rate dependent CV data presented here strongly support the ECE/DISP pathway. This is evidenced by the slopes of E_{pa} (IV/II) vs log(v) extracted from **Figure 2.1b** which indicated regions of kinetic control by both chemical (~30 mV dec^{-1}) and electrochemical steps (~60 mV dec^{-1}) as well as the increase in normalized peak current at low scan rates. For the specific case of an RSD-ECE/DISP pathway, Saveant has shown that the rate constant for the chemical step can be defined further by the relation $k_c = 4k_{LE}[Ni^{II}(dtc)_2]_0$ or $k_c = 2k_{LE}[Ni^{II}(dtc)_2]_0$, where k_{LE} is the second order rate constant for the ligand exchange reaction. The former expression refers to the case where k_{LE} is larger than the disproportionation rate constant (k_D) and represents a true ECE mechanism where $Ni^{III}(dtc)_3$ is oxidized quickly at the electrode surface. The latter expression is reserved for the case where $k_D > k_{LE}$ and represents a DISP1 mechanism. Notably, a third possibility may occur where ligand exchange occurs as a pre-equilibrium to disproportionation. This mechanism is referred to as a DISP2 pathway and exhibits a characteristic E_{pa} vs log(v) slope of 19.7 mV dec^{-1}. Given the observed 29 mV dec^{-1} slope, the DISP2 pathway was not considered further.

Distinguishing between an ECE and DISP1 pathway can be very difficult without knowledge of k_D. Using $k_c = 34$ s^{-1} and $[Ni^{II}(dtc)_2]_0 = 1$ mM, $k_{LE} = 8{,}500$ M^{-1} s^{-1} if an ECE pathway is operative and $k_{LE} = 17{,}000$ M^{-1} s^{-1} if a DISP1 pathway is operative. The disproportionation reaction described as **Equation 7** arises from the difference in redox potentials for the two intermediate Ni^{III} species, $[Ni^{III}(dtc)_2]^+$ and $Ni^{III}(dtc)_3$. Using the reduction potentials in **Scheme 2.1**, $\Delta G^o_{DISP} = -nF(E^o_1 - E^o_4) = -0.49$ eV can be calculated.

The large driving force of the disproportionation step highlights the impact of ligand coordination in determining the redox potential of the metal center. For example, coordination of a third dtc$^-$ ligand to Ni^{III} results in a shift of 0.96 V in the $Ni^{III/II}$ reduction potential from the bis-

coordinated to the tris-coordinated species. This large difference in potentials allows for a potential inversion between E^o_1 and E^o_4, resulting in favorable disproportionation. The key to the observed 2e$^-$ oxidation from $Ni^{II}(dtc)_2$ to $[Ni^{IV}(dtc)_3]^+$ is therefore the large difference in equilibrium constants for ligand exchange, K_2 and K_3. An estimate of K_2 has never been measured in the literature, likely due to its extremely small magnitude, and $[Ni^{II}(dtc)_3]^-$ has never been isolated and characterized. The instability of this species is due to the strong preference of Ni^{II} towards a square planar geometry when coordinated to dtc$^-$ ligands as a result of its d^8 electronic configuration. Fackler has studied the coordination geometries of nickel with 1,1-dithiolate ligands such as dithiocarbamates and xanthates and concluded that strong π-donation from the $-[CS_2]^-$ unit inhibits coordination in the axial position.[54] Notably, $[Fe(dtc)_3]^-$ (d^6) and $[Co(dtc)_3]^-$ (d^7) are stable complexes and CV studies exhibit sequential 1e$^-$ waves for their $M^{IV/III}$ and $M^{III/II}$ redox couples.[55,56]

On the other end of the redox cycle, Ni^{IV} is present in a six-coordinate environment with a low spin electron configuration.[39] Other known examples of Ni^{IV} complexes also exhibit low-spin, six-coordinate geometries.[29,30,57-59] Therefore, the equilibrium constant K_4 in **Scheme 2.1** is expected to be extremely large. Considering **Scheme 2.1** as a whole, we can see that $K_4 >> K_3 >> K_2$ and the regions of stability are titled toward the corners of $Ni^{II}(dtc)_2$ and $[Ni^{IV}(dtc)_3]^+$. The equilibrium K_3 is then critical to the ability to facilitate 1e$^-$ versus 2e$^-$ reactions. If K_3 is small, only the 1e$^-$ $[Ni^{III}(dtc)_2]^+/Ni^{II}(dtc)_2$ process would be observed, however, if K_3 is large, then the ECE mechanism described above would proceed.

Reduction of $[Ni^{IV}(dtc)_3]^+$ back to $Ni^{II}(dtc)_2$ during CV experiments occurs predominately through sequential 1e$^-$ transfer reactions followed by equilibration of $[Ni^{II}(dtc)_3]^-$ to $Ni^{II}(dtc)_2$ (*i.e.* $E^o_4 \rightarrow E^o_3 \rightarrow K_2$ from **Scheme 2.1**). This is due to the relative stability of the tris-chelated $Ni^{III}(dtc)_3$

complex. However, the notable difference in peak currents for the two redox waves suggest some degree of instability. Lachenal proposed that the instability of $Ni^{III}(dtc)_3$ was due to an internal decomposition via oxidation of a dtc^- ligand to yield $Ni^{II}(dtc)_2$ and $dtc^\bullet$. Controlled potential electrolysis of $[Ni^{IV}(dtc)_3]^+$ between E^o_4 and E^o_3 indeed revealed the ultimate production of $Ni^{II}(dtc)_2$ and $(dtc)_2$. However, this reaction involved reduction of $[Ni^{IV}(dtc)_3]^+$ starting material and would necessarily produce uncoordinated dithiocarbamate species.[41] Electrochemical studies presented here with Na[dtc] added to $Ni^{II}(dtc)_2$ solutions showed that irreversible oxidation of dtc^- to $dtc^\bullet$ gave rise to an increase in current for oxidation of $Ni^{III}(dtc)_3$ to $[Ni^{IV}(dtc)_3]^+$. Such an increase indicates that spontaneous and kinetically fast oxidation of $Ni^{II}(dtc)_2$ by $dtc^\bullet$ occurs in homogenous solution to generate $Ni^{III}(dtc)_3$. This reaction is formally the reverse of that proposed by Lachenal and clearly indicates favorability in formation of $Ni^{III}(dtc)_3$, not decomposition.

In the present case where oxidation of $Ni^{II}(dtc)_2$ is followed by reduction of $Ni^{IV}(dtc)_3$ on the return scan, the decomposition of $Ni^{III}(dtc)_3$ must occur on the timescale of CV experiment. We propose that this happens via a reaction between $Ni^{III}(dtc)_3$ and Ni^{II} ions liberated during the oxidation step to regenerate $[Ni^{III}(dtc)_2]^+$. Formally, this reaction is the reverse of the ligand exchange step. Production of $[Ni^{III}(dtc)_2]^+$ then results in either reduction at the electrode surface where the applied potential is now less than E^o_1 or through the disproportionation reaction described in **Equation 7**.

In order to fully describe the complex redox cycle for the $[Ni^{IV}(dtc)_3]^+/Ni^{II}(dtc)_2$ couple, we have used digital simulation software (DigiElch) to model the experimental CV data as a function of scan rate based on **Scheme 2.1.** Known redox potentials E^o_1, E^o_3, and E^o_4 were held constant in addition to the rate constant for electron transfer $k_E = 0.018$ cm s^{-1} determined here for the $[Ni^{III}(dtc)_2]^+/Ni^{II}(dtc)_2$ redox couple and $k_{LE} = 17{,}000$ M^{-1} s^{-1}. A detailed description of the

fitting procedure is provided in the Supporting Information. **Figure 2.7** shows a comparison of experimental cyclic voltammograms for 1 mM $Ni^{II}(dtc)_2$ at 100 and 1000 mV s^{-1} with simulated data overlaid as dashed lines. The agreement between the simulated data and the experimental CVs is excellent with only small differences in the region of the $Ni^{III}(dtc)_3/[Ni^{II}(dtc)_3]^-$ peak. Importantly, the simulated data models the changes in E_{pa} (IV/II), i_{pa} (IV/II), and i_{pc} (III/II) as a function of scan rate quite well.

Based on the simulated data, an equilibrium constant for ligand exchange with Ni^{III} of K_3 = 0.034 ± 0.007 M was calculated. From this value an estimate of K_2 = 3.7 x 10^{-17} M can be reasonably made. The magnitude of K_3 indicates that ligand exchange between $[Ni^{III}(dtc)_2]^+$ and $Ni^{II}(dtc)_2$ (**Equation 5**) is slightly disfavored. We would have expected that $K_3 > 1$ M based on the observed $2e^-$ oxidation and $1e^-$ reduction processes, however, 2e- reactions may still proceed if k_d is sufficiently fast. Indeed, the disproportionation rate constant was best simulated near diffusion limited values and was therefore held constant at 1 x 10^{10} M^{-1} s^{-1}. The large magnitude of this estimate is consistent with the large driving force for disproportionation and supports our use of k_{LE} = 17,000 M^{-1} s^{-1} (DISP pathway) in the simulations. Additionally, the fact that K_3 is close to 1 M is consistent with our proposal of $Ni^{III}(dtc)_3$ decomposition through ligand exchange/disproportionation prior to being reduced at E^o_3 = -0.71 V.

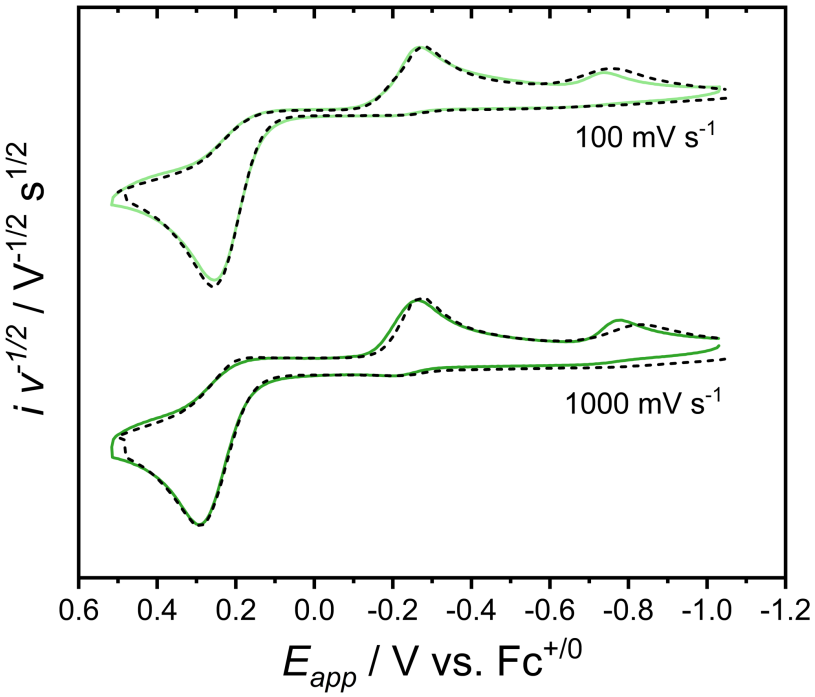

Figure 2.7. Comparison of experimental CV data collected for $Ni^{II}(dtc)_2$ in MeCN (green) with simulated data (black dashed).

Oxidation/Reduction of $Ni^{II}(dtc)_2$ in the presence of pyridine

Addition of pyridine to the MeCN solution resulted in a shift of the $Ni^{II}(dtc)_2$ oxidation peak in the negative direction and an increase in reversibility. The pyridine coupled redox feature can best be described as a $[Ni^{III}(dtc)_2(py)_2]^+/Ni^{II}(dtc)_2$ redox couple where the equilibrium constant for pyridine coordination to $[Ni^{III}(dtc)_2]^+$ was determined to be K = 1.2 (± 0.2) x 10^6 M^{-2}. The negative shift in E_{pa} (III_{py}/II) is characteristic of ligand coupled electron transfer (LCET). The LCET process is analogous to proton coupled electron transfer (PCET) in which reduction of a molecule is coupled with proton transfer in order to stabilize the more electron-rich reduced species. A characteristic result of PCET is a positive shift in the cathodic peak potential for increased $[H^+]$. In the case of $Ni^{II}(dtc)_2$ oxidation, electron density from the coordinated pyridine ligands are necessary to stabilize the electron-deficient Ni^{III} species. Due to this stabilization effect

with added [py], a negative shift in E_{pa} is observed, indicating that oxidation is easier in the presence of pyridine.

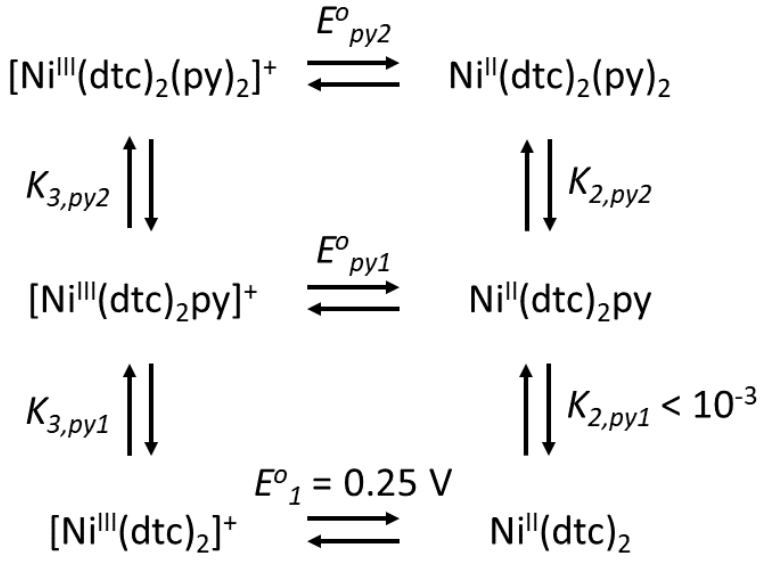

Scheme 2.2. Thermochemical cycle describing $Ni^{III/II}$ reduction potentials as a function of pyridine coordination.

Scheme 2.2 summarizes the effect of pyridine coordination on the $Ni^{III/II}$ reduction potential. Here, the equilibrium constants for pyridine coordination to $[Ni^{III}(dtc)_2]^+$ are described by $K_{3,py1}$ and $K_{3,py2}$, of which the product $K_{3,py1}K_{3,py2} = K = 1.2\ (\pm\ 0.2) \times 10^6\ M^{-2}$. The equilibrium constants for pyridine coordination to $Ni^{II}(dtc)_2$ are smaller than we can detect using UV-Vis and ^1H NMR methods. This was attributed to the strong square planar coordination environment induced by the dithiocarbamate ligands, and has been noted previously in the literature.[54] Based on the observation that the UV-Vis absorbance spectra of $Ni^{II}(dtc)_2$ measured in MeCN and pyridine solvents were identical, indicating <1% pyridine coordination at the solvent concentration of [py] = 12 M, then the equilibrium constant $K_{2,py1}$ can be estimated to be no larger than $10^{-3}\ M^{-1}$. The weak coordination of pyridine to $Ni^{II}(dtc)_2$ indicates that the pyridine coupled oxidation observed by CV must occur through an ECC process with pyridine coordination to

$[Ni^{III}(dtc)_2]^+$ occurring after oxidation. Reduction of $[Ni^{III}(dtc)_2(py)_2]^+$ to $Ni^{II}(dtc)_2$ may occur through either reduction to $Ni^{II}(dtc)_2(py)_2$ followed by rapid dissociation of pyridine ligands (ECC mechanism) or through pyridine dissociation followed by reduction to $Ni^{II}(dtc)_2$ before loss of the second pyridine (CEC mechanism).

The $[Ni^{III}(dtc)_2(py)_2]^+$ complex was found to be unstable at low scan rates, resulting in voltammograms that strongly resemble those without pyridine, but with a shifted anodic wave. The consistency in the appearance of $1e^-$ reduction waves for $[Ni^{IV}(dtc)_3]^+$ and $Ni^{III}(dtc)_3$ at low scan rates indicate that $[Ni^{III}(dtc)_2(py)_2]^+$ must decompose to $[Ni^{IV}(dtc)_3]^+$ under these conditions. The rate constant for this decomposition was measured using the ratio of cathodic to anodic peak currents versus scan rate where the dependence of k_{dec} on pyridine concentration was well described by a competitive parallel reaction mechanism. The two parallel reactions are proposed to be ligand exchange between $Ni^{II}(dtc)_2$ and either six-coordinate $[Ni^{III}(dtc)_2(py)_2]^+$ or five-coordinate $[Ni^{III}(dtc)_2py]^+$.

The rate constant for ligand exchange with $[Ni^{III}(dtc)_2(py)_2]^+$ was determined to be k_2 = 540 M^{-1} s^{-1}, much smaller than the comparative reaction with $[Ni^{III}(dtc)_2]^+$ (17,000 M^{-1} s^{-1}), consistent with the thermodynamic stabilization of Ni^{III} by addition of pyridine as well as the saturation of open coordination sites. The rate constant for ligand exchange with $[Ni^{III}(dtc)_2py]^+$ was not able to be determined directly, however, the relation k_1/K_{py2} = 100 s^{-1} was obtained. Given that $[Ni^{III}(dtc)_2(py)_2]^+$ and $[Ni^{III}(dtc)_2py]^+$ must be present for the parallel reaction mechanism, we can assume that K_{py2} is near unity, but must be greater than 1 based on the overall favorability of $[Ni^{III}(dtc)_2(py)_2]^+$ formation. General estimates of k_1 can therefore be made by assuming a value of K_{py2} such as k_1 = 100 M^{-1} s^{-1} (K_{py2} = 1 M^{-1}), k_1 = 1,000 M^{-1} s^{-1} (10 M^{-1}), and k_1 = 10,000 M^{-1} s^{-1} (100 M^{-1}).

The product of each ligand exchange reaction is proposed to be $Ni^{III}(dtc)_3$ which could undergo further oxidation $[Ni^{IV}(dtc)_3]^+$ either at the electrode surface or through a disproportionation reaction in solution. Additional disproportionation reactions emerge in the presence of pyridine due to the multiple pyridine coordinated Ni^{III} species. **Equations 23-24** describe these pathways. The driving force for disproportionation of the pyridine coordinated species is expected to be much less than that of $[Ni^{III}(dtc)_2]^+$ (ΔG_{DISP} = -0.49 eV). The standard reduction potentials for the $[Ni^{III}(dtc)_2(py)_2]^+/Ni^{II}(dtc)_2(py)_2$ ($E^o_{1,py2}$) and $[Ni^{III}(dtc)_2py]^+/Ni^{II}(dtc)_2py$ ($E^o_{1,py1}$) redox couples are unknown, but are expected to be shifted in a negative direction with respect to E^o_1, thus decreasing the driving force for electron transfer.

(23) $Ni^{III}(dtc)_3 + [Ni^{III}(dtc)_2(py)_2]^+ \rightarrow [Ni^{IV}(dtc)_3]^+ + Ni^{II}(dtc)_2(py)_2$

(24) $Ni^{III}(dtc)_3 + [Ni^{III}(dtc)_2(py)]^+ \rightarrow [Ni^{IV}(dtc)_3]^+ + Ni^{II}(dtc)_2py$

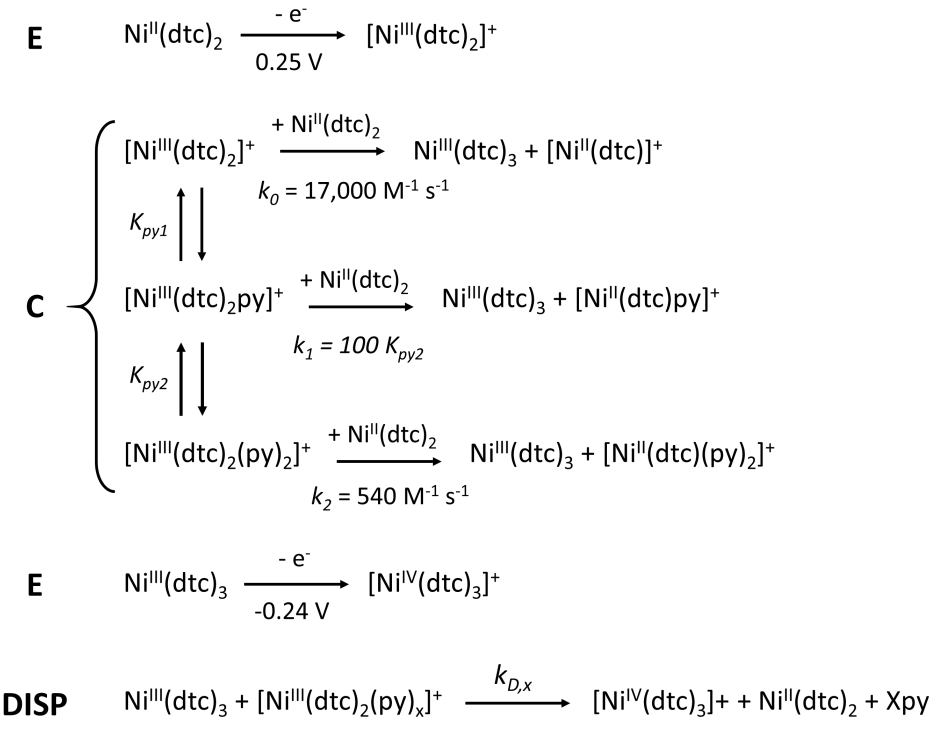

Scheme 2.3. ECE/DISP mechanism describing the oxidation of $Ni^{II}(dtc)_2$ to $[Ni^{IV}(dtc)_3]^+$ in the presence of pyridine.

Scheme 2.3 offers a summary of the reaction pathways for oxidation of $Ni^{II}(dtc)_2$ to $[Ni^{IV}(dtc)_3]^+$ in the presence of pyridine. The mechanism is a modification of that described in the absence of pyridine where $Ni^{II}(dtc)_2$ is first oxidized to $[Ni^{III}(dtc)_2]^+$ with a standard potential of E^o_1 = 0.25 V vs $Fc^{+/0}$. In the absence of pyridine, $[Ni^{III}(dtc)_2]^+$ undergoes ligand exchange with $Ni^{II}(dtc)_2$ to produce $Ni^{III}(dtc)_3$ with a rate constant of $k_{LE} = k_0$ = 17,000 M^{-1} s^{-1} or 17 s^{-1}. Here, k_0 is meant to indicated ligand exchange with zero pyridine ligands. When pyridine is present in solution, rapid coordination of pyridine to $[Ni^{III}(dtc)_2]^+$ is competitive with the k_0 pathway. Formation of $[Ni^{III}(dtc)_2py]^+$ and $[Ni^{III}(dtc)_2(py)_2]^+$ then result in alternative ligand exchange pathways with $Ni^{II}(dtc)_2$, k_1 and k_2, respectively. All three ligand exchange pathways are proposed to result in $Ni^{III}(dtc)_3$ and ultimately yield $[Ni^{IV}(dtc)_3]^+$ through either electrochemical oxidation at E^o_4 = -0.24 V or disproportionation.

Figure 2.9 shows digital simulations based on this mechanism overlaid with experimental CV data collected with [py] = 383 mM. All experimentally obtained rate constants, reduction potentials, and equilibrium constants were fixed during simulations while unknown values were allowed to float to obtain a best fit. The proposed model agrees well with the experimental data but misses some of the data in the region of $Ni^{III}(dtc)_3/[Ni^{II}(dtc)_3]^-$ peak, similar to what was observed in the absence of pyridine. Further understanding of this reduction step is needed in order to refine the model for better fitting in this region. Regardless, the model does an excellent job of fitting the change in reversibility of the $[Ni^{III}(dtc)_2(py)_2]^+/Ni^{II}(dtc)_2$ couple as a function of scan rate.

Given the complexity of the mechanism proposed in **Scheme 2.3** and the limited amount of known thermodynamic and kinetic information, the error associated with fitting parameters such as equilibrium and rate constants are much greater that what was found in the absence of pyridine.

Nonetheless, the simulations support a number of key aspects of the mechanism. Namely, the best fit to the experimental data resulted in equilibrium constants for pyridine coordination of $K_{3,py1}$ = 2.5 x 10^5 M^{-1} and $K_{3,py2}$ = 2 M^{-1}, their product $K_{3,py1}K_{3,py2}$ = 5 x 10^5 M^{-2} being close to the experimental value of 1.2 (± 0.2) x 10^6 M^{-2}. The large disparity in equilibria supports the observation that decomposition of $[Ni^{III}(dtc)_2(py)_2]^+$ occurs through two parallel pathways in which dissociation of a pyridine ligand to form $[Ni^{III}(dtc)_2py]^+$ is an important feature.

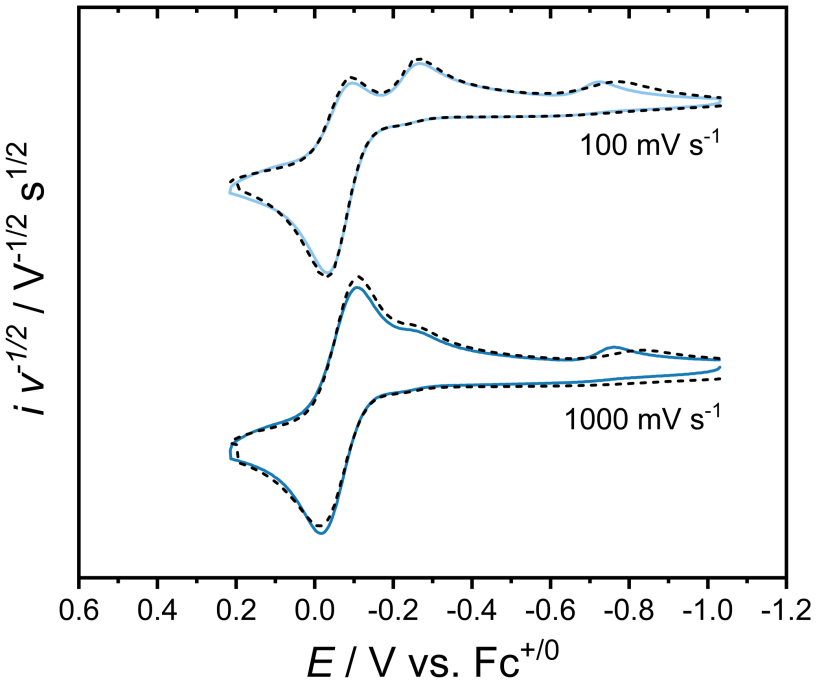

Figure 2.9. Comparison of experimental CV data collected for $Ni^{II}(dtc)_2$ in MeCN with 383 mM pyridine (blue) with simulated data (black dashed).

Ni^{III}-pyridine structure

The structure of the $[Ni^{III}(dtc)_2(py)_2]^+$ complex is presently unknown but we can speculate that the species exists in a six-coordinate environment with either a cis or trans conformation. The high reversibility of the pyridine coupled wave at high scan rates could indicate that a trans conformation is favored, resulting in a lower energy barrier for pyridine coordination. However,

the cis form is more similar to the ultimate structure of $[Ni^{IV}(dtc)_3]^+$ which exists in a tris-chelated octahedral environment. EPR studies were able to confirm the presence of Ni^{III} when both pyridine and oxidant were in solution, however, spectra were highly complex and suggest multiple Ni^{III} species. This could be due to the small equilibrium constant separating the mono- and bis-coordinated pyridine species.

Conclusion

Here we have reported on the impact of pyridine coordination on the multi-electron redox cycle of $Ni^{II}(dtc)_2$. Using cyclic voltammetry we have uncovered a complex mechanism which involves pyridine coordination in the Ni^{III} oxidation state which kinetically inhibits further oxidation to $[Ni^{IV}(dtc)_3]^+$. A comparison of the electrochemical data in the absence and presence of pyridine reveals a common mechanism for oxidation from $Ni^{II}(dtc)_2$ to $[Ni^{IV}(dtc)_3]^+$ based on the RSD-ECE/DISP pathway. We anticipate that MeCN plays a similar role as pyridine in coordination and stabilization of Ni^{III} intermediates. The weakly donating MeCN ligand, however, cannot preserve the coordinated Ni^{III} complex for long enough so as to be detected by CV. These studies suggest that characterization of pyridine coordinated intermediates may be achieved with more strongly donating pyridine derivatives or other coordinating ligands.

References

(1) "Photovoltaic Solar Resource of the United States." Map. Geospatial Data Science, **2012**, NREL, https://www.nrel.gov/gis/solar.html (accessed May 7, 2019).

(2) "United States- Land-Based and Offshore Annual Average Wind Speed at 80 m." Map. Geospatial Data Science, **2006**, NREL, https://www.nrel.gov/gis/wind.html (accessed May 7, 2019).

(3) "Best Research-Cell Efficiency Chart." Chart. Photovoltaic Research, **2019**, NREL, https://www.nrel.gov/pv/cell-efficiency.html (accessed May 7, 2019).

(4) "Solar Power Data for Integration Studies: Alabama." Data. Geospatial Data Science, **2006**, NREL, https://www.nrel.gov/gis/data-solar.html (accessed May 7, 2019).

(5) Li, L.; Kim, S.; Wang, W.; Vijayakumar, M.; Nie, Z.; Chen, B.; Zhang, J.; Xia, G.; Hu, J.; Graff, G.; et al. A Stable Vanadium Redox-Flow Battery with High Energy Density for Large-Scale Energy Storage. *Adv. Energy Mater.* **2011**, *1* (3), 394–400.

(6) Skyllas-Kazacos, M.; Chakrabarti, M. H.; Hajimolana, S. A.; Mjalli, F. S.; Saleem, M. Progress in Flow Battery Research and Development. *J. Electrochem. Soc.* **2011**, *158* (8), R55–R79.

(7) Kazacos, M.; Cheng, M.; Skyllas-Kazacos, M. Vanadium Redox Cell Electrolyte Optimization Studies. *J. Appl. Electrochem.* **1990**, *20* (3), 463–467.

(8) Cabrera, P. J.; Yang, X.; Suttil, J. A.; Hawthorne, K. L.; Brooner, R. E. M.; Sanford, M. S.; Thompson, L. T. Complexes Containing Redox Noninnocent Ligands for Symmetric,

Multielectron Transfer Nonaqueous Redox Flow Batteries. *J. Phys. Chem. C* **2015**, *119* (28), 15882–15889.

(9) Cabrera, P. J.; Yang, X.; Suttil, J. A.; Brooner, R. E. M.; Thompson, L. T.; Sanford, M. S. Evaluation of Tris-Bipyridine Chromium Complexes for Flow Battery Applications: Impact of Bipyridine Ligand Structure on Solubility and Electrochemistry. *Inorg. Chem.* **2015**, *54* (21), 10214–10223.

(10) Sevov, C. S.; Hickey, D. P.; Cook, M. E.; Robinson, S. G.; Barnett, S.; Minteer, S. D.; Sigman, M. S.; Sanford, M. S. Physical Organic Approach to Persistent, Cyclable, Low-Potential Electrolytes for Flow Battery Applications. *J. Am. Chem. Soc.* **2017**, *139* (8), 2924–2927.

(11) Jude, H.; Krause Bauer, J.A.; Connick, W. B. An Outer-Sphere Two-Electron Platinum Reagent. *J. Am. Chem. Soc.* **2003**, *125* (12), 3446-3447.

(12) Lexa, D.; Saveant, J. M. The Electrochemistry of Vitamin B12. *Acc. Chem. Res.* **1983**, *16* (7), 235–243.

(13) Liu, W.; Hempstead, M. R.; Nevin, W. A.; Melník, M.; Lever, A. B. P.; Leznoff, C. C. Disproportionation, Electrochemistry, and Electronic Coupling Involving Mononuclear and Binuclear Cobalt Phthalocyanine Derivatives. *J. Chem. Soc., Dalton Trans.* **1987**, No. 11, 2511–2518.

(14) Waldie, K. M.; Ramakrishnan, S.; Kim, S.-K.; Maclaren, J. K.; Chidsey, C. E. D.; Waymouth, R. M. Multielectron Transfer at Cobalt: Influence of the Phenylazopyridine Ligand. *J. Am. Chem. Soc.* **2017**, *139* (12), 4540–4550.

(15) Boschloo, G.; Hagfeldt, A. Characteristics of the Iodide/Triiodide Redox Mediator in Dye-Sensitized Solar Cells. *Acc. Chem. Res.* **2009**, *42* (11), 1819–1826.

(16) Farnum, B. H.; Jou, J. J.; Meyer, G. J. Visible Light Generation of I–I Bonds by Ru-Tris(Diimine) Excited States. *PNAS* **2012**, *109* (39), 15628–15633.

(17) Gardner, J. M.; Abrahamsson, M.; Farnum, B. H.; Meyer, G. J. Visible Light Generation of Iodine Atoms and I−I Bonds: Sensitized I^- Oxidation and I_3^- Photodissociation. *J. Am. Chem. Soc.* **2009**, *131* (44), 16206–16214.

(18) Farnum, B. H.; Gardner, J. M.; Meyer, G. J. Flash-Quench Technique Employed To Study the One-Electron Reduction of Triiodide in Acetonitrile: Evidence for a Diiodide Reaction Product. *Inorg. Chem.* **2010**, *49* (22), 10223–10225.

(19) Rowley, J. G.; Farnum, B. H.; Ardo, S.; Meyer, G. J. Iodide Chemistry in Dye-Sensitized Solar Cells: Making and Breaking I−I Bonds for Solar Energy Conversion. *J. Phys. Chem. Lett.* **2010**, *1* (20), 3132–3140.

(20) Weng, G.-M.; Li, Z.; Cong, G.; Zhou, Y.; Lu, Y.-C. Unlocking the Capacity of Iodide for High-Energy-Density Zinc/Polyiodide and Lithium/Polyiodide Redox Flow Batteries. *Energy Environ. Sci.* **2017**, *10* (3), 735–741.

(21) Zhang, J.; Jiang, G.; Xu, P.; Kashkooli, A. G.; Mousavi, M.; Yu, A.; Chen, Z. An All-Aqueous Redox Flow Battery with Unprecedented Energy Density. *Energy Environ. Sci.* **2018**, *11* (8), 2010–2015.

(22) Xie, C.; Liu, Y.; Lu, W.; Zhang, H.; Li, X. Highly Stable Zinc–Iodine Single Flow Batteries with Super High Energy Density for Stationary Energy Storage. *Energy Environ. Sci.* **2019**.

(23) Li, B.; Nie, Z.; Vijayakumar, M.; Li, G.; Liu, J.; Sprenkle, V.; Wang, W. Ambipolar Zinc-Polyiodide Electrolyte for a High-Energy Density Aqueous Redox Flow Battery. *Nature Communications* **2015**, *6*, 6303.

(24) Brinkhoff, H. C.; Cras, J. A.; Steggerda, J. J.; Willemse, J. The Oxidation of Dithiocarbamato Complexes of Nickel, Copper and Zinc. *Recueil des Travaux Chimiques des Pays-Bas* **1969**, *88* (6), 633–640.

(25) Fackler, J. P.; Avdeef, Alex.; Fischer, R. G. Structural Characterization of Tris(N,N-Di-n-Butyldithiocarbamato)Nickel(IV) Bromide. A Ni-S6 Complex with Unusual Chemical Properties. *J. Am. Chem. Soc.* **1970**, *92* (23), 6972–6974.

(26) Zilbermann, I.; Maimon, E.; Cohen, H.; Meyerstein, D. Redox Chemistry of Nickel Complexes in Aqueous Solutions. *Chem. Rev.* **2005**, *105* (6), 2609–2626.

(27) Stiefel, E. I.; Waters, J. H.; Billig, E.; Gray, H. B. The Myth of Nickel(III) and Nickel(IV) in Planar Complexes [1]. *J. Am. Chem. Soc.* **1965**, *87* (13), 3016–3017.

(28) Shimada, S.; Rao, M. L. N.; Tanaka, M. Reaction of 1,2-Disilylbenzene with Bis[1,2-Bis(Dimethylphosphino)Ethane]Nickel(0). Isolation and Characterization of the First Silylnickel(IV) Complex. *Organometallics* **1999**, *18* (3), 291–293.

(29) Watson, M. B.; Rath, N. P.; Mirica, L. M. Oxidative C–C Bond Formation Reactivity of Organometallic Ni(II), Ni(III), and Ni(IV) Complexes. *J. Am. Chem. Soc.* **2017**, *139* (1), 35–38.

(30) Chong, E.; Kampf, J. W.; Ariafard, A.; Canty, A. J.; Sanford, M. S. Oxidatively Induced C–H Activation at High Valent Nickel. *J. Am. Chem. Soc.* **2017**, *139* (17), 6058–6061.

(31) Klein, H.-F.; Bickelhaupt, A.; Jung, T.; Cordier, G. Syntheses and Properties of the First Octahedral Diorganonickel(IV) Compounds. *Organometallics* **1994**, *13* (7), 2557–2559.

(32) Klein, H.-F.; Bickelhaupt, A.; Lemke, M.; Sun, H.; Brand, A.; Jung, T.; Röhr, C.; Flörke, U.; Haupt, H.-J. Trimethylphosphine Complexes of Diorganonickel(IV) Moieties. *Organometallics* **1997**, *16* (4), 668–676.

(33) Dimitrov, V.; Linden, A. A Pseudotetrahedral, High-Oxidation-State Organonickel Compound: Synthesis and Structure of Bromotris(1-Norbornyl)Nickel(IV). *Angew. Chem. Int. Ed.* **2003**, *42* (23), 2631–2633.

(34) Carnes, M.; Buccella, D.; Chen, J. Y.-C.; Ramirez, A. P.; Turro, N. J.; Nuckolls, C.; Steigerwald, M. A Stable Tetraalkyl Complex of Nickel(IV). *Angew. Chem. Int. Ed.* **2009**, *48* (2), 290–294.

(35) Martinez, G. E.; Ocampo, C.; Park, Y. J.; Fout, A. R. Accessing Pincer Bis(Carbene) Ni(IV) Complexes from Ni(II) via Halogen and Halogen Surrogates. *J. Am. Chem. Soc.* **2016**, *138* (13), 4290–4293.

(36) D'Accriscio, F.; Borja, P.; Saffon-Merceron, N.; Fustier-Boutignon, M.; Mézailles, N.; Nebra, N. C−H Bond Trifluoromethylation of Arenes Enabled by a Robust, High-Valent Nickel(IV) Complex. *Angew. Chem. Int. Ed.* **2017**, *56* (42), 12898–12902.

(37) Yu, S.; Dudkina, Y.; Wang, H.; Kholin, K. V.; Kadirov, M. K.; Budnikova, Y. H.; Vicic, D. A. Accessing Perfluoroalkyl Nickel(II), (III), and (IV) Complexes Bearing a Readily Attached [C_4F_8] Ligand. *Dalton Trans.* **2015**, *44* (45), 19443–19446.

(38) Bour, J. R.; Camasso, N. M.; Sanford, M. S. Oxidation of Ni(II) to Ni(IV) with Aryl Electrophiles Enables Ni-Mediated Aryl–CF_3 Coupling. *J. Am. Chem. Soc.* **2015**, *137* (25), 8034–8037.

(39) Fackler, J. P.; Avdeef, Alex.; Fischer, R. G. Sulfur Chelates. XVI. Chemical Properties of Oxidized Nickel(II) Dithiocarbamates. X-Ray Crystal Structure of Tris(N,N-Dibutyldithiocarbamato)Nickel(IV)Bromide, $NiC_{27}H_{54}N_3S_6Br$. *J. Am. Chem. Soc.* **1973**, *95* (3), 774–782.

(40) Hendrickson, A. R.; Martin, R. L.; Rohde, N. M. Dithiocarbamates of Nickel in the Formal Oxidation States I-IV. Electrochemical Study. *Inorg. Chem.* **1975**, *14* (12), 2980–2985.

(41) Lachenal, D. Electrochemical Behaviour of Nickel (II) and Ni (IV) N,N-Diethyldithiocarbamates. Synthesis of a Nickel(IV) Species. *Inorg. Nuc. Chem. Lett.* **1975**, *11* (2), 101–106.

(42) Elgrishi, N.; Rountree, K. J.; McCarthy, B. D.; Rountree, E. S.; Eisenhart, T. T.; Dempsey, J. L. A Practical Beginner's Guide to Cyclic Voltammetry. *J. Chem. Educ.* **2018**, *95* (2), 197–206.

(43) Savéant, J.M. *Elements of Molecular and Biomolecular Electrochemistry*; John Wiley & Sons, Ltd, 2006; pp 47.

(44) Basic Research Needs for Solar Energy Utilization. **2005**, Department of Energy.

(45) Wang, W.; Luo, Q.; Li, B.; Wei, X.; Li, L.; Yang, Z. Recent Progress in Redox Flow Battery Research and Development. *Adv. Funct. Mater.* **2013**, *23* (8), 970–986.

(46) Connelly, N. G.; Geiger, W. E. Chemical Redox Agents for Organometallic Chemistry. *Chem. Rev.* **1996**, *96* (2), 877–910.

(47) Andrieux, C. P.; Nadjo, L.; Savéant, J. M. Electrodimerization: VII. Electrode and Solution Electron Transfers in the Radical-Substrate Coupling Mechanism. Discriminative Criteria from the Other Mechanisms in Voltammetric Studies (Linear Sweep, Rotating Disc, Polarography). *Journal of Electroanalytical Chemistry and Interfacial Electrochemistry* **1973**, *42* (2), 223–242.

(48) Nafady, A.; Costa, P. J.; Calhorda, M. J.; Geiger, W. E. Electrochemical Oxidation of $CoCp(CO)_2$: Radical−Substrate Reaction of a 17 e-/18 e- Pair and Production of a Unique Dimer Radical. *J. Am. Chem. Soc.* **2006**, *128* (51), 16587–16599.

(49) Lam, K.; Geiger, W. E. Anodic Oxidation of Disulfides: Detection and Reactions of Disulfide Radical Cations. *J. Org. Chem.* **2013**, *78* (16), 8020–8027.

(50) Elgrishi, N.; Kurtz, D. A.; Dempsey, J. L. Reaction Parameters Influencing Cobalt Hydride Formation Kinetics: Implications for Benchmarking H_2-Evolution Catalysts. *J. Am. Chem. Soc.* **2017**, *139* (1), 239–244.

(51) Lee, C.-M.; Chen, C.-H.; Ke, S.-C.; Lee, G.-H.; Liaw, W.-F. Mononuclear Nickel(III) and Nickel(II) Thiolate Complexes with Intramolecular S−H Proton Interacting with Both Sulfur and Nickel: Relevance to the [NiFe]/[NiFeSe] Hydrogenases. *J. Am. Chem. Soc.* **2004**, *126* (27), 8406–8412.

(52) De Castro, B.; Freire, C. EPR and Electrochemical Study of Nickel(III) Complexes of Bis(3,5-Dichlorosalicylaldehyde) o-Phenylenediimine. Evidence for Adduct Formation with Pyridines. *Inorg. Chem.* **1990**, *29* (25), 5113–5119.

(53) Nicholson, R. S.; Shain, I. Theory of Stationary Electrode Polarography. Single Scan and Cyclic Methods Applied to Reversible, Irreversible, and Kinetic Systems. *Anal. Chem.* **1964**, *36* (4), 706–723.

(54) Coucouvanis, D.; Fackler, J. P. Square-Planar Sulfur Complexes. VI. Reactions of Bases with Xanthates, Dithiocarbamates, and Dithiolates of Nickel(II). *Inorg. Chem.* **1967**, *6* (11), 2047–2053.

(55) Bond, A. M.; Hendrickson, A. R.; Martin, R. L.; Moir, J. E.; Page, D. R. Electrochemical Reduction and Oxidation of Cobalt(III) Dithiocarbamates. *Inorg. Chem.* **1983**, *22* (23), 3440–3446.

(56) Chant, R.; Hendrickson, A. R.; Martin, R. L.; Rohde, N. M. Tris(Dithiocarbamato) Complexes of Iron(II), Iron(III), and Iron(IV). Electrochemical Study. *Inorg. Chem.* **1975**, *14* (8), 1894–1902.

(57) Schultz, J. W.; Fuchigami, K.; Zheng, B.; Rath, N. P.; Mirica, L. M. Isolated Organometallic Nickel(III) and Nickel(IV) Complexes Relevant to Carbon–Carbon Bond Formation Reactions. *J. Am. Chem. Soc*. **2016**, *138* (39), 12928-12934.

(58) Meucci, E. A.; Camasso, N. M.; Sanford, M. S. An Organometalllic NiIV Complex That Participates in Competing Transmetalation and C(Sp2)–O Bond-Forming Reductive Elimination Reactions. *Organometallics* **2017**, *36* (2), 247–250.

(59) Camasso, N. M.; Canty, A. J.; Ariafard, A.; Sanford, M. S. Experimental and Computational Studies of High-Valent Nickel and Palladium Complexes. *Organometallics* **2017**, *36* (22), 4382–4393.

Appendix 1: Supplemental Information

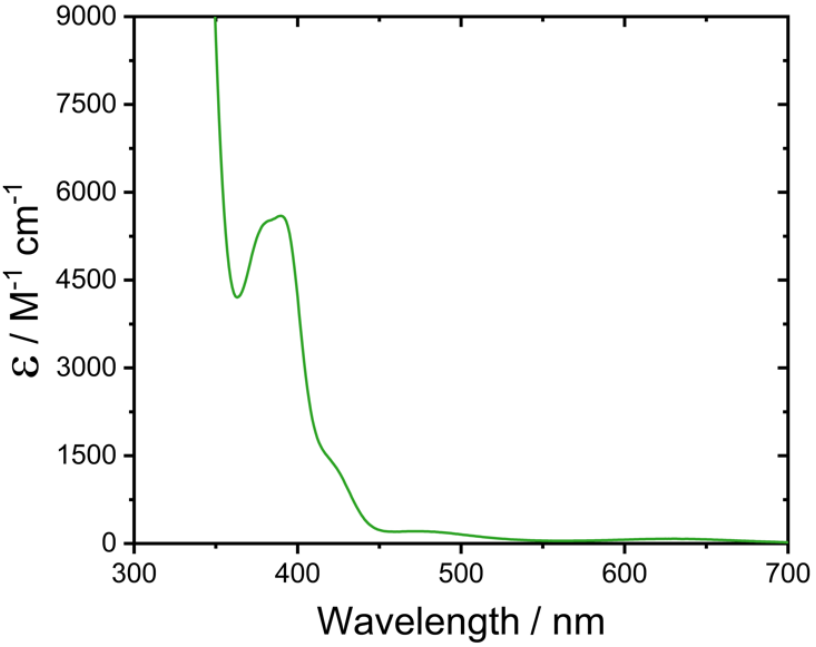

Figure S1. UV-Vis absorbance spectra of $Ni^{II}(dtc)_2$ in MeCN, normalized to the extinction coefficient (M^{-1} cm^{-1}).

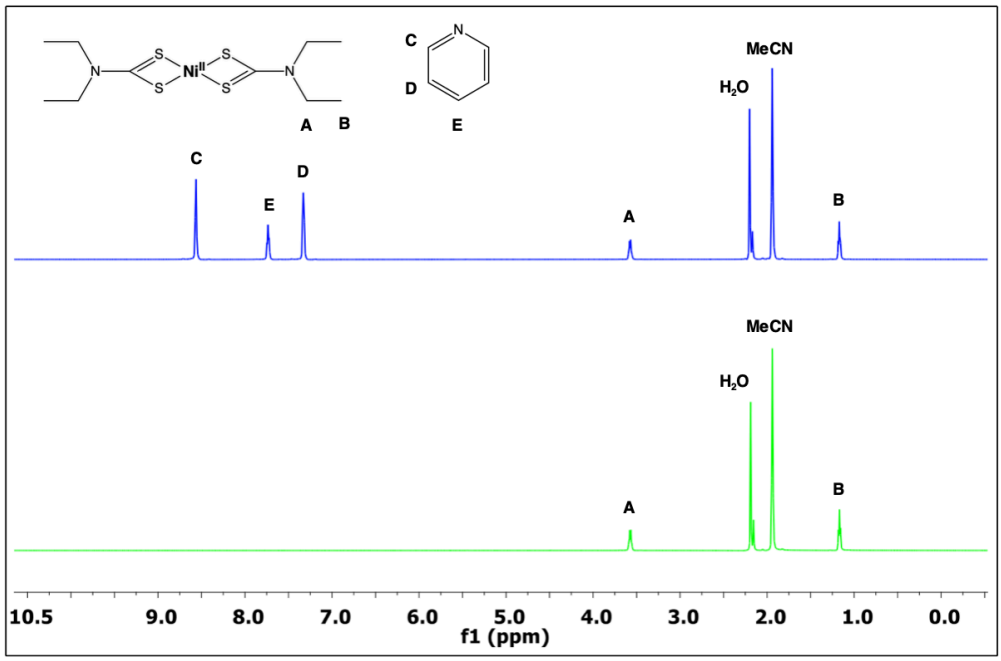

Figure S2. (a) ^{1}H NMR spectrum obtained in d-MeCN at 1 mM $Ni^{II}(dtc)_2$ and 10 mM pyridine. δ 3.57 (q, 2H), 1.17 (t, 3H). Downfield peaks correspond to pyridine protons. (b) ^{1}H NMR spectrum obtained in d-MeCN at 1 mM $Ni^{II}(dtc)_2$. δ 3.57 (q, 2H), 1.17 (t, 3H).

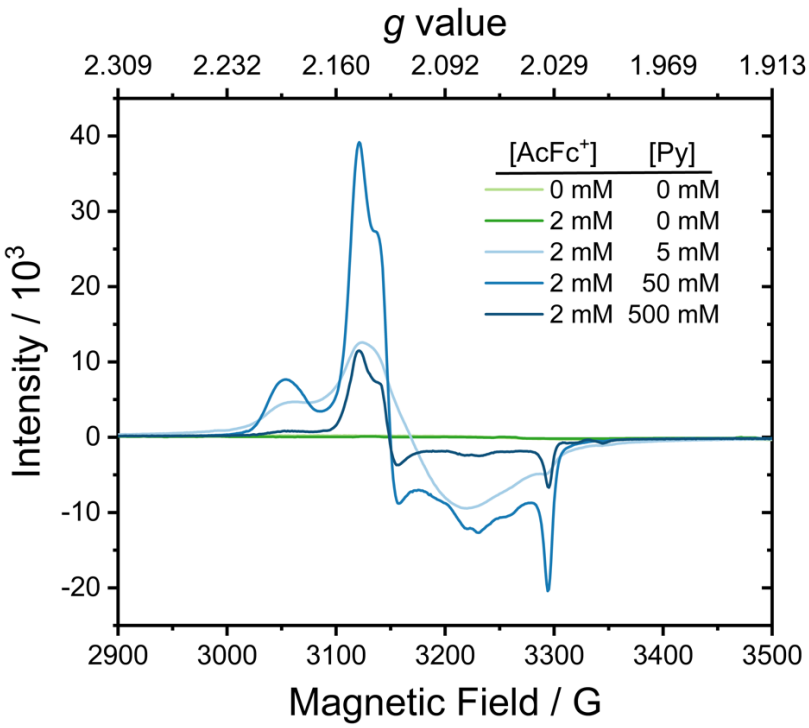

Figure S3. EPR spectra obtained as a function of $AcFc^{+}$ and pyridine concentration. All spectra were recorded in 1 mM $Ni^{II}(dtc)_2$ MeCN at 77 K.

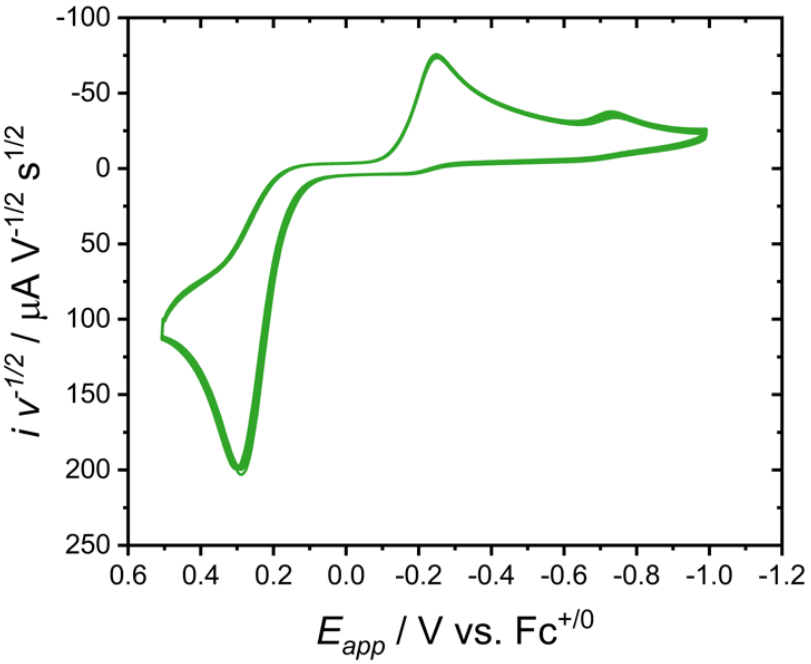

Figure S4. CV of 1 mM $Ni^{II}(dtc)_2$ cycled 100 times in MeCN with 0.1 M $TBAPF_6$ electrolyte at room temperature. Current is normalized to $v^{1/2}$.

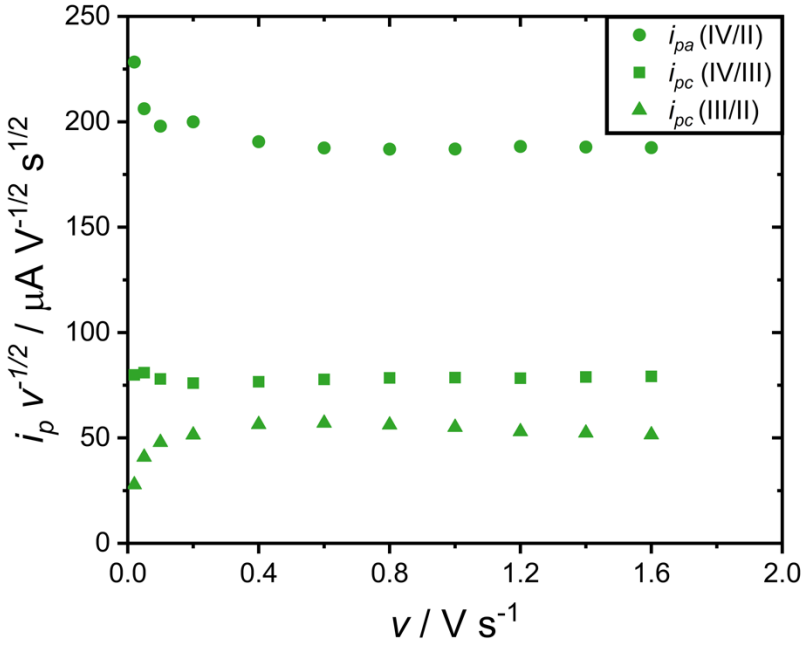

Figure S5. Peak currents (normalized to $v^{1/2}$) as a function of scan rate. Data collected from $Ni^{II}(dtc)_2$ CV traces.

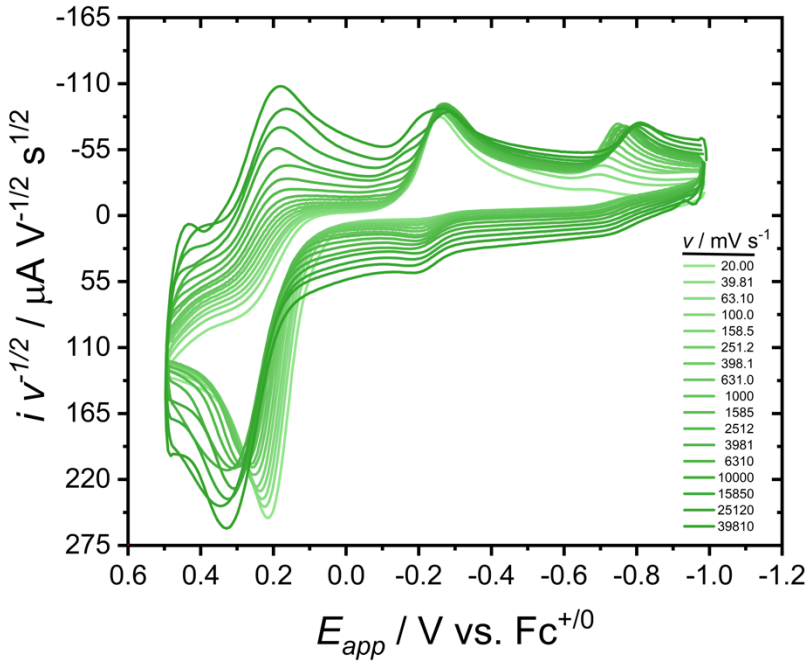

Figure S6. CVs of 1 mM $Ni^{II}(dtc)_2$ in MeCN with 0.1 M $TBAPF_6$ electrolyte at room temperature. Current is normalized to $v^{1/2}$.

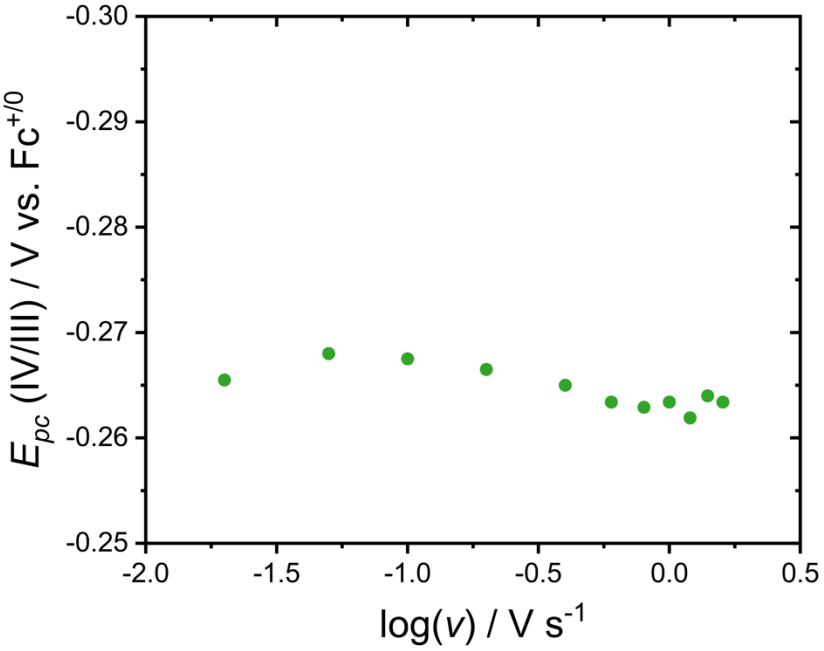

Figure S7. Peak potentials for E_{pc} (IV/III) as a function of scan rate. Data collected from $Ni^{II}(dtc)_2$ CV traces.

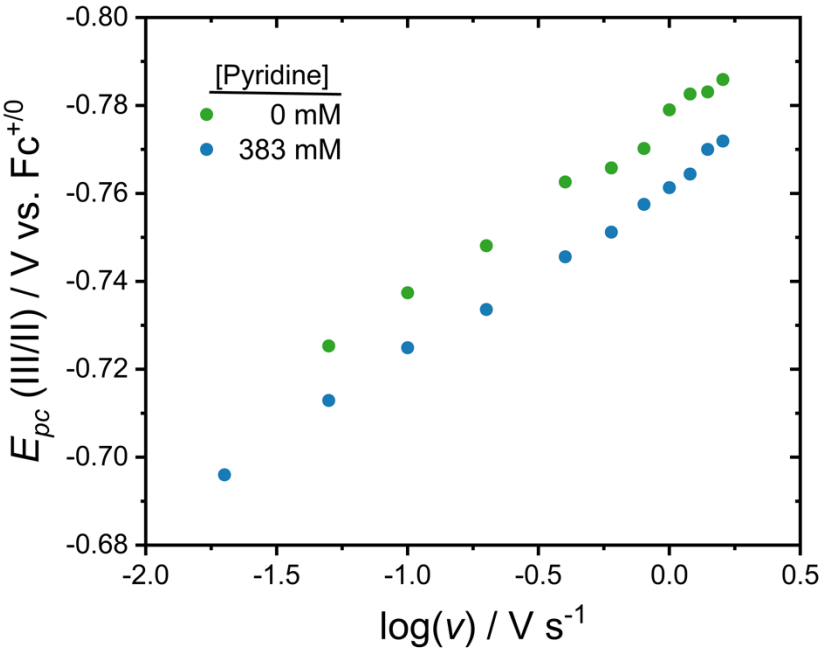

Figure S8. Peak potentials for E_{pc3} (III/II) at 0 and 383 mM pyridine as a function of scan rate. Data collected from $Ni^{II}(dtc)_2$ CV traces.

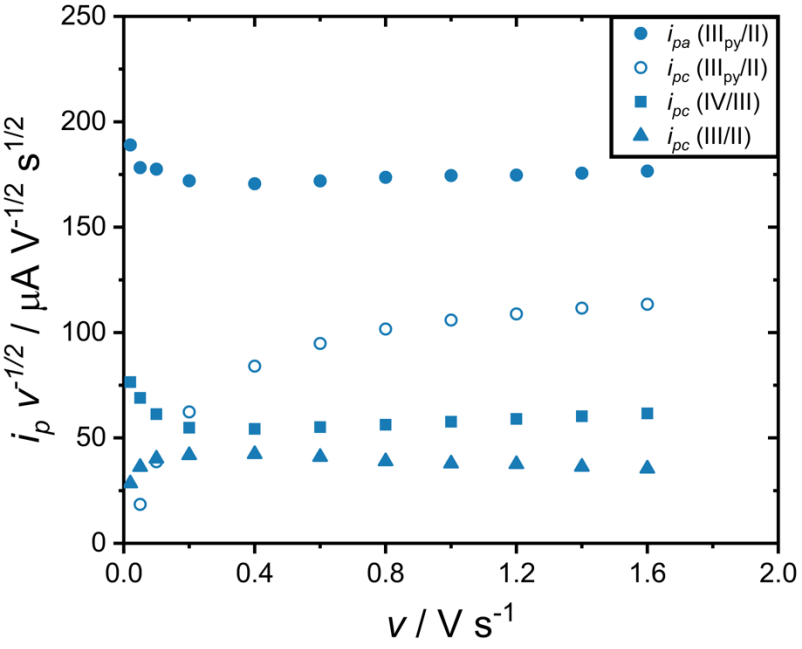

Figure S9. Peak currents (normalized to $v^{1/2}$) at 383 mM pyridine as a function of scan rate. Data collected from $Ni^{II}(dtc)_2$ CV traces.

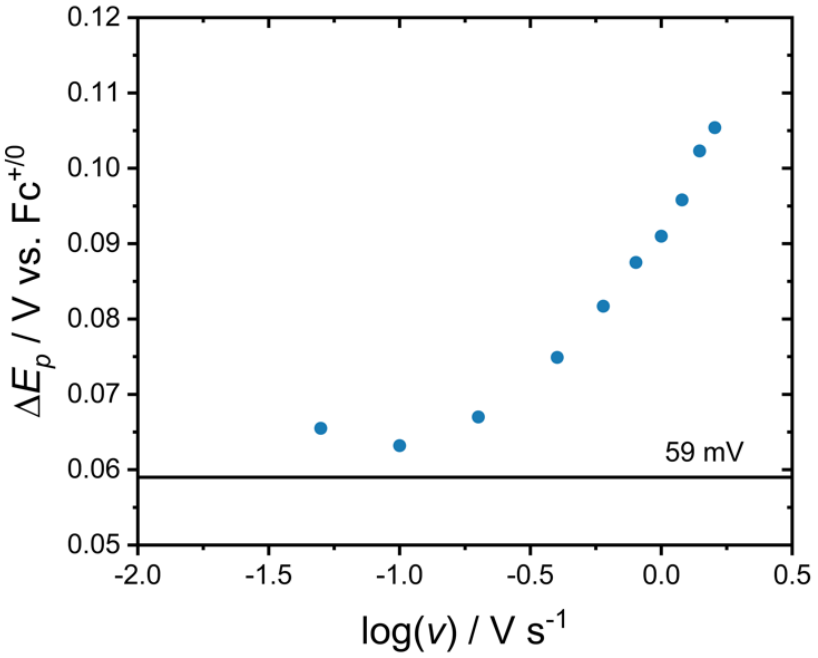

Figure S10. Peak splitting for E_p (III_{py}/II) as a function of scan rate. Data collected from $Ni^{II}(dtc)_2$ CV traces.

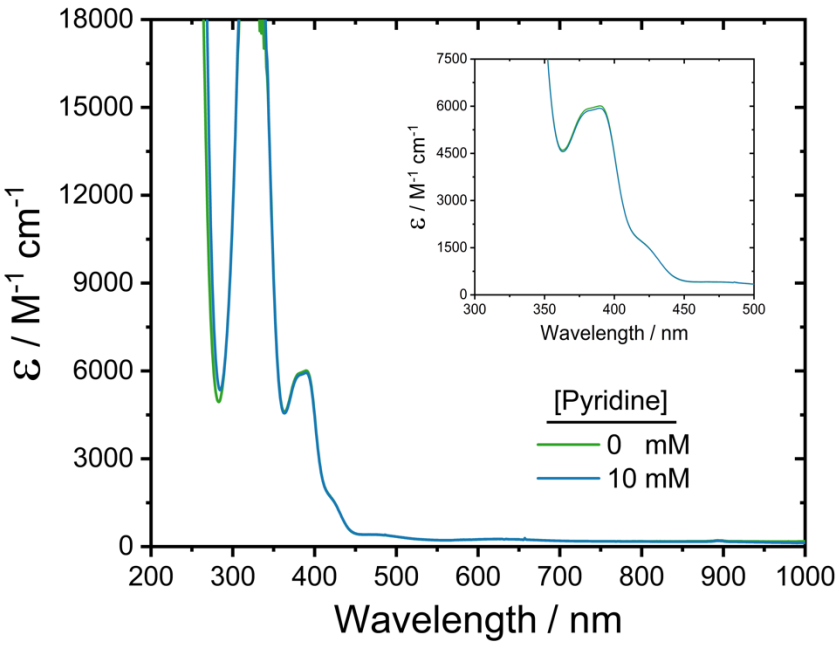

Figure S11. UV-Vis absorbance spectra of 1 mM $Ni^{II}(dtc)_2$ in MeCN, with and without a 10 mM concentration of pyridine.

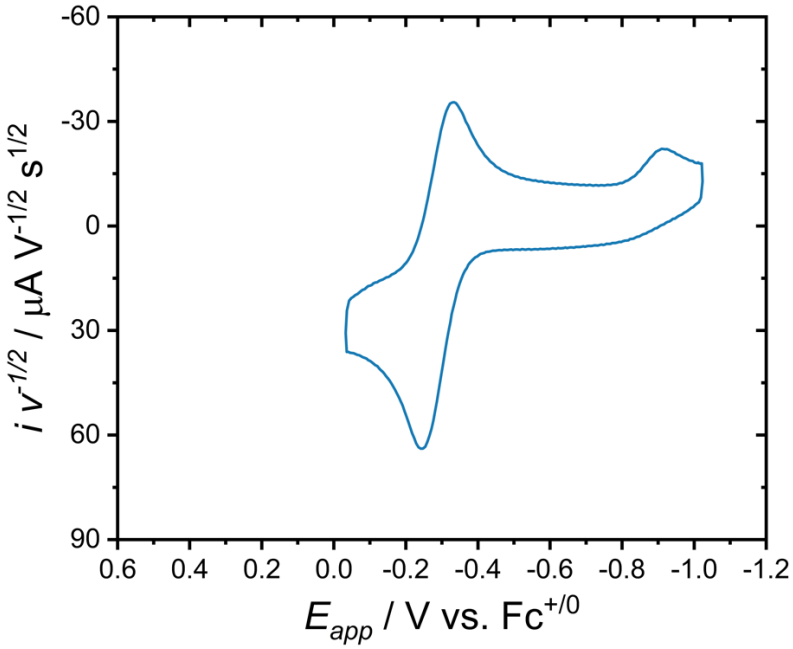

Figure S12. CV of 1 mM $Ni^{II}(dtc)_2$ in pure pyridine with 0.1 M $TBAPF_6$ electrolyte at room temperature. Current is normalized to $v^{1/2}$. Scan rate is 1000 mV s^{-1}.

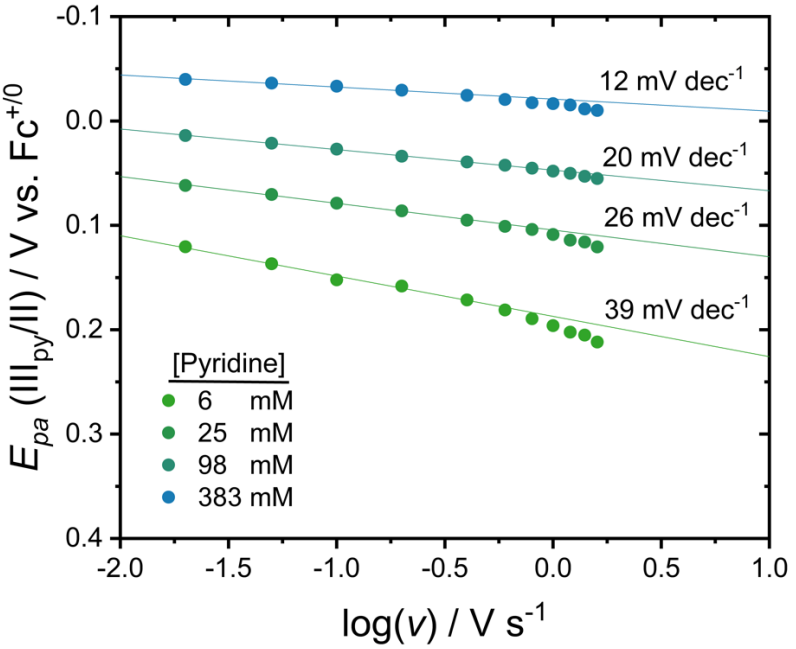

Figure S13. Peak potentials for E_{pa} (III_{py}/II) at 6, 25, 90, and 383 mM pyridine as a function of scan rate. Data collected from $Ni^{II}(dtc)_2$ CV traces. First five data points (chemical step region) used to fit lines.

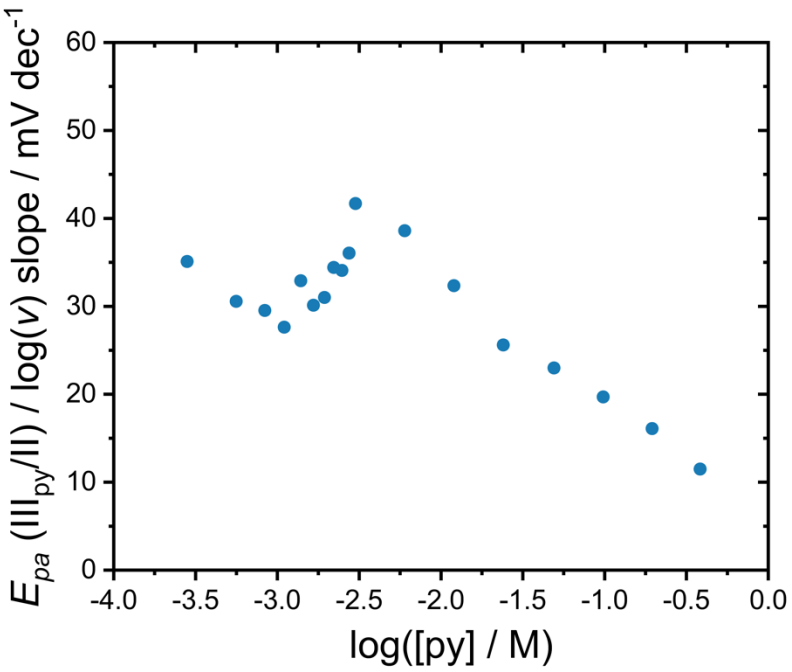

Figure S14. Slopes from fitted lines of E_{pa} (III_{py}/II) versus log(v) as a function of log([py]).

Table S1: E_{pa} for CVs as a Function of Scan Rate and [Pyridine], V vs. $Fc^{+/0}$

	0.02 V/s	0.05 V/s	0.1 V/s	0.2 V/s	0.4 V/s	0.6 V/s	0.8 V/s	1.0 V/s	1.2 V/s	1.4 V/s	1.6 V/s
0 mM	0.235	0.248	0.254	0.262	0.274	0.281	0.287	0.298	0.298	0.300	0.306
3 mM	0.161	0.187	0.207	0.206	0.218	0.225	0.230	0.237	0.242	0.246	0.248
6 mM	0.121	0.137	0.152	0.158	0.172	0.181	0.189	0.196	0.202	0.205	0.212
12 mM	0.092	0.104	0.116	0.123	0.134	0.141	0.145	0.152	0.156	0.159	0.164
25 mM	0.062	0.070	0.079	0.086	0.095	0.101	0.104	0.109	0.114	0.116	0.121
49 mM	0.041	0.050	0.057	0.063	0.071	0.075	0.078	0.080	0.082	0.085	0.088
98 mM	0.014	0.021	0.027	0.034	0.039	0.042	0.045	0.048	0.050	0.053	0.055
195 mM	-0.014	-0.007	-0.002	0.002	0.008	0.002	0.013	0.016	0.019	0.021	0.023
383 mM	-0.040	-0.036	-0.033	-0.030	-0.025	-0.021	-0.018	-0.017	-0.015	-0.012	-0.010

Table S2: E_{pc} for CVs as a Function of Scan Rate and [Pyridine], V vs. $Fc^{+/0}$

	0.02 V/s	0.05 V/s	0.1 V/s	0.2 V/s	0.4 V/s	0.6 V/s	0.8 V/s	1.0 V/s	1.2 V/s	1.4 V/s	1.6 V/s
0 mM	-	-	-	-	-	-	-	-	-	-	-
3 mM	-	-	-	-	0.049	0.049	0.046	0.044	0.038	0.035	0.030
6 mM	-	-	-	0.031	0.042	0.040	0.039	0.037	0.033	0.029	0.025
12 mM	-	-	-	0.023	0.034	0.030	-0.027	0.023	0.020	0.017	0.016
25 mM	-	-	-	0.011	0.011	0.011	-0.007	0.004	0.000	-0.002	-0.005
49 mM	-	-	-0.023	-0.009	-0.009	-0.010	-0.013	-0.016	-0.018	-0.021	-0.022
98 mM	-	-	-0.042	-0.035	-0.037	-0.038	-0.041	-0.045	-0.050	-0.050	-0.052
195 mM	-	-0.077	-0.066	-0.064	-0.067	-0.070	-0.071	-0.076	-0.078	-0.079	-0.082
383 mM	-	-0.102	-0.097	-0.097	-0.100	-0.102	-0.105	-0.108	-0.111	-0.114	-0.116

Table S3: $E_{1/2}$ for CVs as a Function of Scan Rate and [Pyridine], V vs. $Fc^{+/0}$

	0.02 V/s	0.05 V/s	0.1 V/s	0.2 V/s	0.4 V/s	0.6 V/s	0.8 V/s	1.0 V/s	1.2 V/s	1.4 V/s	1.6 V/s
0 mM	-	-	-	-	-	-	-	-	-	-	-
3 mM	-	-	-	-	0.133	0.137	0.138	0.141	0.140	0.140	0.139
6 mM	-	-	-	0.094	0.107	0.111	0.114	0.117	0.118	0.117	0.119
12 mM	-	-	-	0.073	0.084	0.086	0.059	0.088	0.088	0.088	0.090
25 mM	-	-	-	0.049	0.053	0.056	0.049	0.056	0.057	0.057	0.058
49 mM	-	-	0.017	0.027	0.031	0.032	0.032	0.032	0.032	0.032	0.033
98 mM	-	-	-0.007	0.000	0.001	0.002	0.002	0.002	0.000	0.002	0.002
195 mM	-	-0.042	-0.034	-0.031	-0.030	-0.034	-0.029	-0.030	-0.029	-0.029	-0.030
383 mM	-	-0.069	-0.065	-0.063	-0.062	-0.062	-0.061	-0.062	-0.063	-0.063	-0.063

Table S4: ΔE_p for CVs as a Function of Scan Rate and [Pyridine], V

	0.02 V/s	0.05 V/s	0.1 V/s	0.2 V/s	0.4 V/s	0.6 V/s	0.8 V/s	1.0 V/s	1.2 V/s	1.4 V/s	1.6 V/s
0 mM	-	-	-	-	-	-	-	-	-	-	-
3 mM	-	-	-	-	0.169	0.177	0.184	0.193	0.204	0.211	0.218
6 mM	-	-	-	0.128	0.130	0.141	0.151	0.159	0.169	0.176	0.186
12 mM	-	-	-	0.100	0.100	0.111	0.172	0.129	0.136	0.142	0.149
25 mM	-	-	-	0.075	0.084	0.090	0.111	0.105	0.114	0.118	0.125
49 mM	-	-	0.080	0.071	0.080	0.085	0.091	0.096	0.100	0.106	0.110
98 mM	-	-	0.069	0.069	0.076	0.081	0.086	0.093	0.100	0.103	0.107
195 mM	-	0.070	0.064	0.066	0.074	0.072	0.084	0.091	0.097	0.101	0.105
383 mM	-	0.066	0.063	0.067	0.075	0.082	0.088	0.091	0.096	0.102	0.105

Table S5: i_{pa0} for CVs as a Function of Scan Rate and [Pyridine], µA

	0.02 V/s	0.05 V/s	0.1 V/s	0.2 V/s	0.4 V/s	0.6 V/s	0.8 V/s	1.0 V/s	1.2 V/s	1.4 V/s	1.6 V/s
0 mM	32.29	46.10	62.58	89.43	120.5	145.3	167.3	187.1	206.3	222.5	237.5
3 mM	28.25	39.70	52.60	74.79	104.4	127.0	147.9	165.8	181.3	195.3	209.4
6 mM	27.33	38.46	52.89	73.50	100.8	122.0	141.1	158.7	174.4	189.0	203.5
12 mM	28.40	39.98	55.40	78.56	105.6	126.4	145.0	161.2	176.1	190.8	203.5
25 mM	28.37	42.24	57.48	79.73	108.2	130.5	150.2	166.4	182.4	197.0	210.4
49 mM	28.88	42.60	58.00	81.67	113.5	137.6	157.5	176.3	193.6	209.4	224.0
98 mM	29.43	43.15	58.71	82.78	113.6	138.7	160.3	180.0	197.3	212.3	227.8
195 mM	29.01	43.10	57.56	81.69	112.9	138.2	160.0	179.6	197.1	213.8	229.0
383 mM	26.73	39.86	56.15	76.93	107.9	133.2	155.3	174.5	191.4	207.8	223.4

Table S6: i_{pc0} for CVs as a Function of Scan Rate and [Pyridine], µA

	0.02 V/s	0.05 V/s	0.1 V/s	0.2 V/s	0.4 V/s	0.6 V/s	0.8 V/s	1.0 V/s	1.2 V/s	1.4 V/s	1.6 V/s
0 mM	-	-	-	-	-	-	-	-	-	-	-
3 mM	-	-	-	2.67	7.738	14.60	21.99	29.70	37.57	45.44	52.91
6 mM	-	-	-	3.332	11.54	21.22	30.98	40.58	50.09	58.92	67.75
12 mM	-	-	-	4.419	15.51	27.84	39.96	51.33	62.43	72.67	82.26
25 mM	-	-	1.695	7.391	22.24	37.23	51.28	64.65	77.07	88.30	98.90
49 mM	-	-	2.650	10.21	27.89	45.41	61.20	76.36	90.15	102.7	114.4
98 mM	-	-	5.000	14.95	36.47	56.18	73.49	89.23	103.5	116.0	128.6
195 mM	-	2.200	8.124	21.66	46.13	66.70	84.71	100.4	114.8	127.9	140.0
383 mM	-	4.122	12.25	27.89	53.15	73.45	90.94	105.9	119.2	132.0	143.5

Table S7: i_{pc0}/i_{pca0} for CVs as a Function of Scan Rate and [Pyridine]

	0.02 V/s	0.05 V/s	0.1 V/s	0.2 V/s	0.4 V/s	0.6 V/s	0.8 V/s	1.0 V/s	1.2 V/s	1.4 V/s	1.6 V/s
0 mM	-	-	-	-	-	-	-	-	-	-	-
3 mM	-	-	-	0.0357	0.0741	0.1150	0.1487	0.1791	0.2072	0.2327	0.2527
6 mM	-	-	-	0.0453	0.1145	0.1739	0.2196	0.2557	0.2872	0.3118	0.3329
12 mM	-	-	-	0.0563	0.1469	0.2203	0.2756	0.3184	0.3545	0.3809	0.4042
25 mM	-	-	0.0295	0.0927	0.2056	0.2853	0.3414	0.3885	0.4225	0.4482	0.4701
49 mM	-	-	0.0457	0.1250	0.2457	0.3300	0.3886	0.4331	0.4657	0.4905	0.5107
98 mM	-	-	0.0852	0.1806	0.3210	0.4051	0.4585	0.4957	0.5246	0.5464	0.5645
195 mM	-	0.0510	0.1411	0.2652	0.4086	0.4826	0.5294	0.5590	0.5825	0.5982	0.6114
383 mM	-	0.1034	0.2182	0.3625	0.4926	0.5514	0.5856	0.6069	0.6228	0.6352	0.6424

Table S8: i_{pc}/i_{pa} for CVs as a Function of Scan Rate and [Pyridine] as Obtained by Nicholson's Method

	0.02 V/s	0.05 V/s	0.1 V/s	0.2 V/s	0.4 V/s	0.6 V/s	0.8 V/s	1.0 V/s	1.2 V/s	1.4 V/s	1.6 V/s
0 mM	-	-	-	-	-	-	-	-	-	-	-
3 mM	-	-	-	0.2819	0.3257	0.3634	0.3988	0.4276	0.4494	0.4730	0.494
6 mM	-	-	-	0.3369	0.4011	0.4597	0.5045	0.5463	0.5816	0.6129	0.6388
12 mM	-	-	-	0.3611	0.4551	0.5322	0.5916	0.6342	0.6721	0.7048	0.7259
25 mM	-	-	0.3007	0.3591	0.4834	0.5757	0.6430	0.6957	0.7385	0.7684	0.7968
49 mM	-	-	0.2990	0.3843	0.5269	0.6223	0.6849	0.7449	0.7858	0.8182	0.8452
98 mM	-	-	0.3293	0.4310	0.5697	0.6621	0.7276	0.7721	0.8034	0.8249	0.8496
195 mM	-	0.28332	0.3664	0.4964	0.6455	0.7234	0.7749	0.8079	0.8355	0.8612	0.8762
383 mM	-	0.30927	0.4435	0.5631	0.6991	0.7654	0.8069	0.8310	0.8480	0.8645	0.8768

Table S9: K_{eq} at Varying Scan Rates, 10^6 M^{-2}

	K_{eq}
0.1 V/s	1.21
0.2 V/s	1.19
0.4 V/s	1.16
0.6 V/s	0.95
0.8 V/s	1.12
1.0 V/s	1.62
1.2 V/s	1.27
1.4 V/s	1.23
1.6 V/s	1.33

Measurement of k_{dec} from ECE/DISP working curve

A working curve was constructed from DigiElch software using an RSD-ECE/DISP mechanism described below. The rate constants used for the working curve specifically apply to the DISP1 regime where $k_D > k_c$. The substrate concentration was set to [A] = 0.001 M and the voltage scan limit was set to be 0.25 V past E^o(A/B) in order to match the limits used for the experimental data. The value of the scan limit is important in determining the maximum uncorrected current ratio under reversible conditions. A larger scan limit would increase the current ratio while a smaller limit would decrease the current ratio.

$A \rightarrow B + e^-$ E
$B + A \rightarrow C$ C (k_c)
$C \rightarrow D + e^-$ E
$B + C \rightarrow D + A$ DISP (k_D)
$2A \rightarrow D + 2e^-$ NET

Electrochemical Steps	E^o / V	α	k_s / cm s^{-1}
$B + e^- \rightarrow A$	0.25	0.5	1
$D + e^- \rightarrow C$	-0.25	0.5	1
Chemical Steps	K_{eq}	k_f / M^{-1} s^{-1}	k_b
$B + A \rightarrow C$	1	1	1 s^{-1}
$B + C \rightarrow D + A$	3 x 10^8	1 x 10^{10}	33 M^{-1} s^{-1}

Table S10 shows the standard working curve data used for analysis where the maximum uncorrected current ratio was ~0.72. Given that $\lambda = (k_{dec}/v)*(RT/nF)$, then $\log(v) = \log(nF/RT\lambda) + \log(k_{dec})$. Decomposition rate constants were extracted from experimental data by adding an appropriate $\log(k_{dec})$ value to the $\log(v)$ x-data set, thus shifting the working curve until it visually overlaid the experimental data.

Table S10: Standard Curve Data

Log(λ)	Log(v) (k_{dec} = 1 s^{-1})	i_c/i_a
8.55E-06	2993.842	0.71945
1.71E-05	1496.921	0.71938
2.57E-05	997.9472	0.71968
5.13E-05	498.9736	0.71979
8.55E-05	299.3842	0.71942
1.71E-04	149.6921	0.71903
2.57E-04	99.79472	0.71849
5.13E-04	49.89736	0.72379
8.55E-04	29.93842	0.71429
0.00171	14.96921	0.70866
0.00257	9.97947	0.70236
0.00513	4.98974	0.68549
0.00855	2.99384	0.66373
0.0171	1.49692	0.61368
0.02565	0.99795	0.56978
0.05131	0.49897	0.46356
0.08551	0.29938	0.36468
0.17102	0.14969	0.22469
0.25653	0.09979	0.15262
0.51305	0.0499	0.05944
0.85509	0.02994	0.01604
1.71018	0.01497	0
2.56527	0.00998	0
5.13053	0.00499	0
8.55089	0.00299	0
17.10177	0.0015	0
25.65266	9.98E-04	0
51.30532	4.99E-04	0
85.50887	2.99E-04	0
171.0177	1.50E-04	0
256.5266	9.98E-05	0

Kinetic Influence of Pyridine on k_{dec}

Reaction Scheme

(1) $[Ni^{III}(dtc)_2(py)_2]^+ + Ni^{II}(dtc)_2 \rightarrow Ni^{III}(dtc)_3 + [Ni^{II}(dtc)(py)_2]^+$ k_2

(2) $[Ni^{III}(dtc)_2(py)_2]^+ \rightleftharpoons [Ni^{III}(dtc)_2py]^+ + py$ $1/K_{3,py2} = k_{-py2}/k_{+py2}$

(3) $[Ni^{III}(dtc)_2(py)]^+ + Ni^{II}(dtc)_2 \rightarrow Ni^{III}(dtc)_3 + [Ni^{II}(dtc)(py)]^+$ k_1

$[Ni^{III}L_2py]^+$ Rate Law (L = dtc)

$$-\frac{d[Ni^{III}L_2py]}{dt} = k_1[Ni^{II}L_2][Ni^{III}L_2py]_{ss} + k_{+py}[py][Ni^{III}L_2py]_{ss} - k_{-py}[Ni^{III}L_2py_2] = 0$$

$$[Ni^{III}L_2py]_{ss} = \frac{k_{-py}[Ni^{III}L_2py_2]}{k_1[Ni^{II}L_2] + k_{+py}[py]}$$

$[Ni^{III}L_2py_2]^+$ Rate Law (L = dtc)

$$-\frac{d[Ni^{III}L_2py_2]}{dt} = k_2[Ni^{II}L_2][Ni^{III}L_2py_2] - k_{-py}[Ni^{III}L_2py_2] + k_{+py}[py][Ni^{III}L_2py]_{ss}$$

$$-\frac{d[Ni^{III}L_2py_2]}{dt} = \left\{k_2[Ni^{II}L_2] - k_{-py} + \frac{k_{+py}[py]k_{-py}}{k_1[Ni^{II}L_2] + k_{+py}[py]}\right\}[Ni^{III}L_2py_2]$$

$$-\frac{d[Ni^{III}L_2py_2]}{dt} = \left\{k_2[Ni^{II}L_2] + \frac{k_1[Ni^{II}L_2]k_{-py}}{k_1[Ni^{II}L_2] + k_{+py}[py]}\right\}[Ni^{III}L_2py_2]$$

$$\boldsymbol{k_{obs} = k_2[Ni^{II}L_2] + \frac{k_1[Ni^{II}L_2]k_{-py}}{k_1[Ni^{II}L_2] + k_{+py}[py]}}$$

Eliminating variables…

$$k_{obs} = k_2[Ni^{II}L_2] + \left(\frac{k_1[Ni^{II}L_2]k_{-py}}{k_1[Ni^{II}L_2] + k_{+py}[py]}\right)\left(\frac{K_{py}}{K_{py}}\right)$$

$$\boldsymbol{k_{obs} = k_2' + \frac{k_1'k_{-py}}{k_1' + k_{-py}[py]}}$$

$$\boldsymbol{k_2' = k_2[Ni^{II}L_2]} \qquad \boldsymbol{k_1' = (k_1/K_{3,py2})[Ni^{II}L_2]}$$

DigiElch Simulations

General Note: Digital simulations of CV data were performed with DigiElch 8.0 software using mechanisms described below for the absence and presence of pyridine. Experimentally determined reduction potentials and rate constants were held constant during fitting. Rate constants for electrochemical steps were not allowed to exceed 1 cm s^{-1}. Rate constants for chemical steps which were allowed to float were not allowed to exceed diffusion limited conditions (*i.e.* 10^{10} M^{-1} s^{-1}). Electron transfer coefficients (α) were held constant at 0.5.

Experimentally determined values are shown in **bold**. Floating variables are shown with errors reported as +/- one standard deviation as determined by DigiElch software. Variables which exceeded reasonable limitations and were therefore fixed at limiting values are shown in *italics*. Values that were fixed to satisfy k_1' (yet the ratio of which were determined experimentally) are given an asterisk. Variables which were calculated by DigiElch based on other variables (fixed or floating) are shown in plain text with no error.

Absence of Pyridine: Electrochemical and Chemical steps are defined below. Values which exceed their reasonable limitations were the electron transfer rate constant for Reaction 2 (fixed at 1 cm s^{-1}) and the disproportionation rate constant for Reaction 5 (fixed at 1 x 10^{10} M^{-1} s^{-1}).

Electrochemical Steps	E^o / V	α	k_s / cm s^{-1}
1. $[Ni^{III}(dtc)_2]^+ + e^- \rightarrow Ni^{II}(dtc)_2$	**0.25**	0.5	**0.018**
2. $[Ni^{IV}(dtc)_3]^+ + e^- \rightarrow Ni^{III}(dtc)_3$	**-0.24**	0.5	*1*
3. $Ni^{III}(dtc)_3 + e^- \rightarrow [Ni^{II}(dtc)_3]^-$	**-0.71**	0.5	0.0025 (± 0.0003)
Chemical Steps	K_{eq}	k_f / M^{-1} s^{-1}	k_b / M^{-1} s^{-1}
4. $[Ni^{III}(dtc)_2]^+ + Ni^{II}(dtc)_2 \rightarrow Ni^{III}(dtc)_3 + [Ni^{II}(dtc)]^+$	3.4 (±0.7) x 10^{-2}	**1.7 x 10^4**	4.9 x 10^5
5. $[Ni^{III}(dtc)_2]^+ + Ni^{III}(dtc)_3 \rightarrow Ni^{II}(dtc)_2 + [Ni^{IV}(dtc)_3]^+$	1.9 x 10^8	*1 x 10^{10}*	52
6. $[Ni^{II}(dtc)]^+ + [Ni^{II}(dtc)]^+ \rightarrow Ni^{II}(dtc)_2 + Ni^{II}$	75 (±14)	4.5 (±0.5) x 10^3	60
7. $[Ni^{II}(dtc)_3]^- + Ni^{II} \rightarrow Ni^{II}(dtc)_2 + [Ni^{II}(dtc)]^+$	6.5 x 10^{15}	0.4 (±3.7) x 10^9	6.2 x 10^{-8}

Presence of Pyridine: CVs for [py] = 383 mM were modeled using Electrochemical and Chemical steps defined below *in addition* to the reactions defined above for the absence of pyridine.

Electrochemical Steps	E^o / V	α	k_s / cm s^{-1}
8. $[Ni^{III}(dtc)_2py]^+ + e^- \rightarrow Ni^{II}(dtc)_2py$	-0.25	0.5	1
9. $[Ni^{III}(dtc)_2(py)_2]^+ + e^- \rightarrow Ni^{II}(dtc)_2(py)_2$	-0.16	0.5	1
Chemical Steps	K_{eq}	k_f / M^{-1} s^{-1}	k_b
10. $[Ni^{III}(dtc)_2]^+ + py \rightarrow [Ni^{III}(dtc)_2py]^+$	2.5 (±0.1) x 10^5 M^{-1}	1 x 10^{10}	3.9 x 10^4 s^{-1}
11. $[Ni^{III}(dtc)_2py]^+ + py \rightarrow [Ni^{III}(dtc)_2(py)_2]$	**2*** M^{-1}	14	**7.2** s^{-1}
12. $Ni^{II}(dtc)_2 + py \rightarrow Ni^{II}(dtc)_2py$	**1 x 10^{-3}** M^{-1}	6.2 (±5.6) x 10^4	6.2 x 10^7 s^{-1}
13. $Ni^{II}(dtc)_2py + py \rightarrow Ni^{II}(dtc)_2(py)_2$	64 (±63) M^{-1}	3.2 (±4.1) x 10^7	5.0 x 10^5 s^{-1}
14. $[Ni^{II}(dtc)py]^+ + py \rightarrow [Ni^{II}(dtc)(py)_2]^+$	32 M^{-1}	1 x 10^{10}	3.1 x 10^8 s^{-1}
15. $[Ni^{III}(dtc)_2py]^+ + Ni^{II}(dtc)_2 \rightarrow Ni^{III}(dtc)_3 + [Ni^{II}(dtc)py]^+$	0.077 (±2.3)	**200***	2.6 x 10^3 M^{-1} s^{-1}
16. $[Ni^{III}(dtc)_2(py)_2]^+ + Ni^{II}(dtc)_2 \rightarrow Ni^{III}(dtc)_3 + [Ni^{II}(dtc)(py)_2]^+$	1.2 (±3.9)	**540**	440 M^{-1} s^{-1}
17. $[Ni^{III}(dtc)_3]^- + [Ni^{II}(dtc)(py)_2]^+ \rightarrow Ni^{II}(dtc)_2 + Ni^{II}(dtc)_2(py)_2$	1.7 x 10^9	1 x 10^{10}	5.9 M^{-1} s^{-1}
18. $[Ni^{III}(dtc)_2py]^+ + Ni^{III}(dtc)_3 \rightarrow Ni^{II}(dtc)_2py + [Ni^{IV}(dtc)_3]^+$	0.75	1.6 (±14) x 10^5	2.1 x 10^5 M^{-1} s^{-1}
19. $[Ni^{III}(dtc)_2(py)_2]^+ + Ni^{III}(dtc)_3 \rightarrow Ni^{II}(dtc)_2(py)_2 + [Ni^{IV}(dtc)_3]^+$	24	0.063 (±7.3) x 10^5	26 M^{-1} s^{-1}